AFRL-SR-BL-TR-98-

0287

# REPORT DOCUMENTATION PAGE



| 1. AGENCY USE ONLY (Leave blank) | 2. REPORT DATE | 3. REPORT TYPE AND DATES COVERED |
|---|---|---|
| | Feb. 12, 1998 | Final Technical - 15 Jul 97-14 Nov. 97 |

**4. TITLE AND SUBTITLE**
Kinetic and Transport Models for Nonequilibrium Hydrogen/Nitrogen Plasma Propellants

**5. FUNDING NUMBERS**
F49620-97-1-0223
$80,758

**6. AUTHOR(S)**
Dr. Dennis Keefer, PhD

**7. PERFORMING ORGANIZATION NAME(S) AND ADDRESS(ES)**
University of Tennessee Space Institute
B.H. Goethert Parkway
Tullahoma, TN 37388

**8. PERFORMING ORGANIZATION REPORT NUMBER**

**9. SPONSORING/MONITORING AGENCY NAME(S) AND ADDRESS(ES)**
AFOSR/NA
110 Duncan Avenue, Suite B115
Bolling AFB, DC 20332-0001

N/A

**10. SPONSORING/MONITORING AGENCY REPORT NUMBER**

**11. SUPPLEMENTARY NOTES**

**12a. DISTRIBUTION/AVAILABILITY STATEMENT**
Approved for public release; distribution is unlimited

**12b. DISTRIBUTION CODE**

19980414 065

**13. ABSTRACT** *(Maximum 200 words)*

A cascade arc facility was developed to study the characteristics of nonequilibrium plasma propellants for electric propulsion applications. The cascade arc was operated with hydrogen arcs at 2.0 and 6.0 psi. Spatially resolved spectral emission data were collected using a two dimensional Optical Multichannel Analyzer (OMA). Electron density was determined by fitting theoretical line profiles to experimentally measured Abel inverted emission line profiles. Radial distributions of plasma temperature were estimated from Boltzmann plots of spectral line intensity. The measured electron densities and plasma temperatures were compared to values predicted by nonequilibrium cascade arc simulations using the UTSI Cascade Arc Plasma Simulation (CAPS) code. The simulations underpredicted the peak experimental electron densities by as much as an order of magnitude and over predicted peak plasma temperatures by as much as a factor of 2.5. The experimental electric field has been accurately predicted by varying chemical kinetics in the CAPS code. Kinetic models developed at the University of Illinois gave the best agreement with the Cascade Arc measurements and are the best chemical kinetics tested for hydrogen. Electron number density profiles for simulated ammonia and hydrazine were also obtained at pressures of 2.0, 6.0, and 10.0 psi. A hydrogen/nitrogen mixture version of the CAPS code is under development that will enable evaluation of candidate finite rate kinetic models for these propellants.

| 14. SUBJECT TERMS | 15. NUMBER OF PAGES |
|---|---|
| Nonequilibrium plasmas, hydrogen/nitrogen, cascade arc, stark effect, spectroscopy | 37 |
| | 16. PRICE CODE |

| 17. SECURITY CLASSIFICATION OF REPORT | 18. SECURITY CLASSIFICATION OF THIS PAGE | 19. SECURITY CLASSIFICATION OF ABSTRACT | 20. LIMITATION OF ABSTRACT |
|---|---|---|---|
| unclassified | unclassified | unclassified | UL |

## EXECUTIVE SUMMARY

A cascade arc facility has been constructed at The University of Tennessee Space Institute (UTSI) to study the effect of nonequilibrium transport properties in hydrogen-nitrogen electric propulsion propellant plasmas. The ability to accurately simulate electric thruster flows has been limited by the lack of validated finite rate kinetic models and nonequilibrium transport properties. Measurements of plasma properties in the cascade arc are being used to guide development of the physical models required for further development of electric propulsion thruster computational codes. The cascade arc has been operated on hydrogen with a current of 50 A at pressures of 2.0 psi and 6.0 psi. Spatially resolved spectral data at these conditions have been collected for the Balmer $H_\alpha$, $H_\beta$, $H_\gamma$, and $H_\delta$ lines. The experimental $H_\alpha$ lineshapes have been fitted to theoretical lineshapes to determine the degree of Stark broadening. This allows the radial distributions of electron number density to be determined. Radial profiles of an equilibrium plasma temperature have also been estimated from Boltzmann plots using the line emission from $H_\alpha$, $H_\beta$, $H_\gamma$, and $H_\delta$ lines. Candidate kinetic models were evaluated by comparing computer predictions using the UTSI Cascade Arc Plasma Simulation (CAPS) code with measurements of the plasma properties in the arc.

The CAPS code simulations have been run with a wide range of chemical kinetic models. The simulated plasma conditions were found to be extremely sensitive to the kinetics. The predicted nonequilibrium electron number densities underpredicted the experimental values by as much as an order of magnitude and overpredicted the experimental values by as much as a factor of two, depending on the kinetics model utilized and the arc pressure. The peak electron densities were consistently overpredicted by the equilibrium solutions. The experimental electric fields were bounded by the nonequilibrium computer simulations by using different finite rate chemical kinetic rates. The "U of I" finite rate chemical kinetic model matches the experimental electric field and best predicts the distribution of electron number densities. Even though the "U of I" rates do not exactly match the measured electron densities, the uncertainty associated with the experimental electron number densities makes it very difficult to claim that the electron densities predicted by the "U of I" simulations are incorrect. The "U of I" chemical kinetic rate set, therefore, is believed to be the best finite rate chemical kinetics set tested for hydrogen. In addition to the measured distributions of electron number densities, Boltzmann plots have been used to determine a rough estimate for the radial distribution of plasma electron temperature. These preliminary experimental temperature data are overpredicted by the simulations by as much as 2.5 times.

Cascade arc measurements have also been obtained for simulated ammonia and simulated hydrazine. Electron number density profiles for have been obtained for 50 Amp arcs at 2 psi, 6 psi, and 10 psi. A hydrogen/nitrogen mixture version of the CAPS code is under development that will enable evaluation of candidate finite rate kinetic models for these important propellants.

Cumulative List of Professional Personnel:

Dennis Keefer
Trevor Moeller
Robert Rhodes
Newton Wright
Fred Schwartz
James Hornkohl
Thomas Walloschek

Publications:
T. Moeller, D. Keefer, and R. Rhodes, "Cascade Arc Studies of Nonequilibrium Hydrogen Plasmas," AIAA 96-3294, 32nd AIAA/ASME/SAE/ASEE Joint Propulsion Conference, Lake Buena Vista, FL, July 1-3, 1996.

T. Moeller, D. Keefer, and R. Rhodes, " Studies of Nonequilibrium Hydrogen/Nitrogen Plasmas using a Cascade Arc," AIP Conference Proceedings 387, p. 317, The Space Technology and Applications International Forum (STAIF-97), Albuquerque, NM, Jan. 1997.

T. Moeller, D. Keefer, and R. Rhodes, "Nonequilibrium Hydrogen/Nitrogen Plasmas Studies Using a Cascade Arc," IEPC 97-063, 25th International Electric Propulsion Conference, Cleveland, OH, August, 1997.

Theses and Dissertations:
Trevor Moeller, "Cascade Arc Studies of Nonequilibrium Hydrogen/Nitrogen Plasmas," Ph.D. dissertation, The University of Tennessee Space Institute, expected May 1998. The major findings in this dissertation are presented in this final report. This dissertation will be available from the University of Tennessee in May 1998.

## 1.0 INTRODUCTION

Electric propulsion thrusters offer significant advantages for satellite station keeping and maneuvering, since their specific impulse can be more than twice that of conventional resistojet or chemical thrusters that are commonly used for these missions. Computational codes can be used to guide refinements in the configuration of electric propulsion thrusters that lead to better thruster performance. A number of computer simulation codes have been developed for this purpose [1-4]. However, it is now clear that there are important nonequilibrium processes in the propellant plasma that must be understood before adequate physical models can be constructed for use in these computational codes. A cascade arc facility has been constructed at The University of Tennessee Space Institute (UTSI) that permits accurate diagnostic measurements of nonequilibrium propellant plasma properties. These measurements are used to evaluate the kinetic models and transport properties required for further development of the computational codes.

### 1.1 USE OF THE CASCADE ARC FOR NONEQUILIBRIUM PLASMA RESEARCH

Some of the most important chemical and transport processes in the propellant plasmas of electric propulsion thrusters, e.g. radial species diffusion and recombination, occur on time scales that are comparable to the convection times in these thrusters. This fast convection produces the strong axial gradients found in the propellant plasma. Therefore, the plasma conditions at a given point in a thruster depend strongly on the previous history of the plasma passing through that point. Comparison of code predictions with measurements in this case requires that the entire upstream flow field be accurately predicted. Differences between measured and predicted quantities could be due to inaccuracies in the models at any point upstream of the measurement location. This makes it very difficult to assess which model mechanisms or rates should be altered to improve the code.

Cascade arcs have long been used as a means to measure the fundamental atomic constants and transport properties of high temperature gases [5]. The cascade arc has a flow velocity much smaller than seen in electric propulsion thrusters, and the length of the arc plasma in the cascade is tens of diameters as compared to one diameter that is typical in electric propulsion devices. This produces plasmas with properties similar to propellant plasmas in electric propulsion thrusters but with negligible axial gradients. The radial temperature profiles in the cascade arc are controlled primarily by diffusive transport properties rather than convection. In the cascade arc, where there are no significant axial gradients, a balance between radial diffusion and chemical reactions with an axially constant but radially dependent energy input determines the nonequilibrium plasma parameters. The plasma properties depend on the local conditions at the measurement station rather than a complex space-time convolution of all the conditions upstream of the point of measurement. Differences observed between code predictions and measured quantities are more easily related to the specific reactions or diffusion rates which must be modified to improve the code models.

## 2.0 UTSI CASCADE ARC FACILITY

The UTSI cascade arc is comprised of individually water-cooled copper plates separated by electrical insulators (Figure 1). These plates are 3.175 mm (1/8 ") thick and form a 4 mm diameter arc channel that is approximately 40 mm long. The insulators are ceramic paper or mica 0.254 mm (0.010") thick. A modified water-cooled copper plate with windows allows optical access. This section is located in the center of the cascade arc to minimize end effects. The cathode is a 6.35 mm (0.250") diameter thoriated tungsten rod with a 60 degree cone on the end. The anode is 9.144 mm (0.360") diameter thoriated tungsten rod with a blunt end. A water jet impinging on their back surfaces cools both electrodes. The arc is driven by a 50 A, 600 V power supply. A cascaded centrifugal pump delivers 41.64 liters/min (11 gal/min) of water at 1.38 MPa (200 psi) to cool the copper plates and electrodes. The cascade arc is positioned vertically to eliminate arc asymmetries caused by buoyancy.

Accurate measurement of plasma parameters requires careful integration of the external optics with the design of the central window section. Abel inversion of the emission data is needed to provide radial measurements of the plasma properties [6]. An adjustable, reflective Cassegrain optical collection system is used. to provide a small entrance solid angle for the cascade window section and to avoid off-axis aberrations. This collects light from the arc and directs it into a 1.25 meter focal length spectrometer so that the primary mirror in the spectrometer is overfilled (Figure 2). Figure 3 is a photograph of the UTSI Cascade Arc Facility. Before entering the Cassegrain telescope the light from the arc is rotated ninety degrees so that the radial dimension of the arc image lies along the slit. A two-dimensional optical multichannel analyzer (OMA) with image intensifier is used to collect and digitize the data. This detector has a 512 x 512 pixel detector array with 19 μm pixel spacing and is used to acquire simultaneous spectral data at many radial locations. The magnification of the optical system is approximately 1.0 providing 200 pixel resolution across the 4 mm diameter arc channel. Further details of the experimental setup were presented at the AIAA 32nd Joint Propulsion Conference [7].

## 3.0 EXPERIMENTAL PROCEDURE AND DATA REDUCTION

The cascade arc was operated with pure hydrogen arcs at 2.0 psi and 6.0 psi and a current of 50 Amps. Spectral emission data from the 656.28 nm Balmer alpha, $H_\alpha$, line in the 8th order were collected using a 1.25 m Spex spectrometer with a 316 groove/mm echelle grating and a two-dimensional OMA detector [7]. Nine images of the arc were collected at each pressure. A 1.9 N.D. filter and a 550 nm high-pass filter were utilized to prevent detector saturation and eliminate interference from higher order lines, respectively. The OMA detector exposure times were 0.2 seconds for the 6.0 psi case and 2.0 seconds for the 2.0 psi case. The 2.0 psi case required longer exposure times because the intensity of the radiation was lower. The images of the arc have 512 spectral pixels and 400 spatial pixels. Wavelength calibration was performed on the spectral pixels using atomic lines from a low-density neon calibration source. The spatial pixels were calibrated by taking images of a 50 μm vertical slit backlit by the neon lamp and placed in the same position as the arc when the cascade is in operation. By moving the vertical slit across the location of the arc with a precision translation table, the spatial pixels were associated with a radial position across the arc region. The spectrometer slit function was

experimentally measured using a narrow neon spectral line, and the measured spectral lines were spectrally deconvolved using a digital Wiener filter [8].

Because the Stark effect has strong dependence on electron number densities and depends only slightly on temperature, the electron number density of a plasma can be determined independently of the plasma temperature by comparing theoretical line widths to the experimentally measured $H_\alpha$ lines [6]. The 2-D OMA captures spectral intensity data at many spatial locations across the arc simultaneously. Because this intensity data is a line-of-sight projection of the emission data onto a one-dimensional plane, it must be Abel inverted to obtain radial profiles of the spectral emission. Theoretical line widths can then be compared to this radial distribution of spectral lines to determine the radial variation of electron number density.

The Abel inversion is performed using a modern approach that utilizes integral transforms [10]. In this method, the Abel inversion of line-of-sight intensity data into radially distributed emission data is accomplished by taking the Fourier transform of the intensity data and then performing an inverse Hankel transform. A method for determining the center of the data is incorporated in this inversion technique that minimizes asymmetries. Because Abel inversion implies radial symmetry, any asymmetry is assumed to be noise. Since the Fourier transform of symmetric data is real and the Fourier transform of asymmetric data has imaginary components, the imaginary components of asymmetric data are noise, by definition. Therefore, by shifting the data so that the imaginary components of the transform are minimized, the center can be found. Because fast Fourier transforms (FFT's) can be implemented in the method described above, this Abel inversion process can be performed much faster than conventional methods.

The following algorithm has been used to implement this Abel inversion approach in our data analysis. (1) A fast Fourier transform (FFT) is performed on the intensity data. (2) High frequency noise is filtered out of spectral data using an optimal, finite impulse response (FIR), low band pass filter.(3) The inverse fast Fourier transform (IFFT) is performed on the data. These first three steps smooth the spectral data by filtering out high frequency noise. The Abel inversion is performed next. (4) Perform FFT on spatial data. (5) Filter spatial high frequency noise using another FIR, low band pass filter. (6) Center transformed data by shifting to minimize imaginary component of transformed data. (7) Discard the imaginary part of the shifted, transformed data. This step eliminates noise (asymmetries) in the data. (8) Perform the inverse Hankel transform to obtain the Abel inverted data.

After Abel inversion, a radial distribution of broadened emission profiles is obtained. At the pressures tested, both Doppler and Stark effects can broaden the lines. The resulting line profile is a Voigt profile--a convolution of Gaussian (Doppler) and Lorentzian (Stark) lineshapes. A downhill simplex computer algorithm [11] was used to fit a Voigt profile to the experimental data. From this fitting routine, line widths for both the Lorentzian and Gaussian components of the Voigt profile were determined. Plasma line broadening theory was used to correlate the width of the Stark component to the electron number density. Broadening due to the Stark effect has been calculated using two assumptions about ion motion [6,12]. The first assumption states that the ions have a very small velocity compared to the electrons. This assumption implies that the broadening due to atomic collisions with ions is insignificant compared broadening due to the atomic collisions with electrons. The second assumption relaxes the stationary ion restriction,

and therefore includes excitation of atoms through collisions with moving ions. In general, the dynamic ion assumption results in better fits to the emission line and significantly broader line widths for the same electron number density [12].

To obtain estimates of plasma electron temperature distributions in the 50 A hydrogen arcs at 2 psi and 6 psi, emission profiles of the $H_\alpha$, $H_\beta$, $H_\gamma$, and $H_\delta$ lines were used to make radially resolved Boltzmann plots. The emission profiles were obtained using the Abel inversion technique described above. This data was collected in the second order to guarantee an accurate estimate of the continuum. A standard tungsten filament lamp was used to calibrate the spectral sensitivity of the detector over the range defined by these spectral lines.

Further details of the experimental procedure were presented at the AIAA 32nd Joint Propulsion Conference [7] , the 1st Conference on Synergistic Power and Propulsion Systems Technology [9], and the 25th International Electric Propulsion Conference [13]. This experiment has been repeated for simulated ammonia and simulated hydrazine at pressures of 2 psi, 6 psi, and 10 psi. Detector exposure times of 2 seconds were used for these measurements. Results are shown in Sections 5 and 6.

## 4.0 THE UTSI CASCADE ARC PLASMA SIMULATION (CAPS) CODE

The equilibrium and nonequilibrium UTSI arcjet computer codes have been modified into one-dimensional nonequilibrium and equilibrium Cascade Arc Plasma Simulation (CAPS) codes [14]. At present these codes model a $H_2$, $H$, $H^+$, $e$ hydrogen system. Both codes include radiation transport. The nonequilibrium version includes species diffusion and a finite rate chemistry kinetic model and uses a two-temperature model with separate energy equations for heavy species and electrons. In both codes it is assumed that the pressure is constant, the radial velocity is zero, and the radial current density is zero. The required mass flow is assured by adjustment of velocity levels. The consequence of these assumptions is that species production and diffusion are locally balanced and total production is balanced by wall losses for the axial momentum, energy, electron energy, and species. The transport properties for both the equilibrium and nonequilibrium versions of the UTSI cascade arc computer code are calculated using a computer code written by Cho based on the procedures developed by DeVoto [15].

### 4.1 The Numeric Model and Governing Equations

The algorithm for the solution of the governing equations in the CAPS code is the same as that used in the UTSI arcjet simulation code [14]; however, the CAPS code assumptions mentioned above greatly simplify the governing equations. These governing equations are discussed in this section. The algorithm for the CAPS code is a Navier-Stokes solver based on the SIMPLE (Semi-implicit Pressure Linked Equation) algorithm developed by Gosman and Pun [16] and modified by Rhie [17] to accommodate both supersonic and subsonic flow. Jeng [18, 19] and Rhodes [20] incorporated a magnetic field equation coupled with heat release to study laser heat addition and radio frequency heating of a plasma, respectively. The code is formulated to solve the steady-state Navier-Stokes equations. The governing equations in the code are solved in a

transformed coordinate where the original, non-orthogonal, axially symmetric grid is mapped to a grid of unit squares [21].

The computation grid representing the UTSI Cascade Arc is shown in Figure 4. The axial dimension is along the abscissa and the radial dimension is along the ordinate. The grid point density increases near the wall to aid code convergence in regions where radial gradients can be large. The CAPS code uses the program control and array structure used in the UTSI arcjet simulation code. As a result, the CAPS code computation grid has an axial dimension, even though conservation equations are solved only in the radial direction. The conservation equations are solved for grid cells in the transformed computation grid (see Figure 5).

The SIMPLE algorithm used in the CAPS code is a solver for equations of the form:

$$\nabla \cdot \rho \vec{v} \varphi = \nabla \cdot \Gamma_{\varphi} \nabla \varphi + S \qquad (1)$$

where $\varphi$ represents the axial velocity (u), the static enthalpy (H), the electron temperature ($T_e$ for nonequilibrium), and species concentrations ($\alpha_i$ for nonequilibrium). $\Gamma$ represents the transport coefficient appropriate for each variable. Any terms that cannot be put into a convective or diffusive form are added to the source term, S. The transformation of the grid coordinates into a grid of unit squares results in mixed derivatives from diffusive terms that are also added to S [14]. Second order accurate finite difference representations are used to represent equation (1) for the variable under consideration at each point in the computation grid. Written in matrix form, these coupled equations result in a tri-diagonal matrix that is solved using a tri-diagonal solver. Equation (1) is solved for each of the dependent variables using under-relaxation. Updated values of the dependent variables are used when they are available, and old values are used when the variables have yet to be updated. The process of solving equation (1) for each of the dependent variables is repeated until the sum of the all of the residual errors has reduced to an acceptably small value [14]. At this point the numerical solution to the problem is no longer changing significantly.

### 4.1.1 Equilibrium/Nonequilibrium Momentum Equation

The form of the momentum conservation equation is the same for both the equilibrium and nonequilibrium cases. The axial velocities are obtained from the momentum equation for steady, axially symmetric flow [21]. The momentum equation in vector form is [22]

$$\nabla \cdot \rho \vec{v} \cdot \vec{v} = \nabla \cdot \mu \nabla \vec{v} - \nabla p - \nabla \times \left( \mu \nabla \times \vec{v} \right) + J \times B \qquad (2)$$

Where $\rho$ is the density, **v** is the velocity of the gas (**v** is equal to the axial velocity), p is the pressure, $\mu$ is the viscosity, **J** is the current density, which only has an axial component, and **B** is the magnetic field. Because of the constant pressure assumption, the pressure force term, $-\nabla p$, is zero. The Lorentz body force term, $\mathbf{J} \times \mathbf{B}$, is indirectly zero because of assumptions in the code. Since the current has only an axial component and the magnetic field only has an azimuthal

component, the cross product of **J** and **B** is in the radial direction. The flow in the cascade is assumed to be axial; therefore, the Lorentz force in the radial direction has no effect on the momentum equation (only the axial momentum equation is solved in this problem). The momentum equation solved in the CAPS code is

$$\nabla \cdot \rho \vec{v} \cdot \vec{v} = \nabla \cdot \mu \nabla \vec{v} - \nabla \times \left( \mu \nabla \times \vec{v} \right) \tag{3}$$

As mentioned above, the momentum equation is the same for both the equilibrium and the nonequilibrium versions of the code.

### 4.1.2 Equilibrium Energy Equation

The equilibrium CAPS code assumes local thermodynamic equilibrium (LTE). This assumption implies that the temperature of all of the particles in the gas is the same. Therefore, only one energy equation is necessary to describe a plasma in LTE. The static enthalpy, H, is obtained from the following energy equation, which includes ohmic heating, radiation loss, and viscous dissipation [22].

$$\nabla \cdot \rho \vec{v} H = \nabla \cdot \frac{k}{C_p} \nabla H + \Phi + q_i - q_r + \vec{v} \cdot \nabla p \tag{4}$$

where

$\Phi$ = viscous dissipation,

$$\Phi = \mu \left[ 2\left(\frac{\partial u}{\partial x}\right)^2 + \left(\frac{\partial u}{\partial r}\right)^2 - \frac{2}{3}\left(\frac{\partial u}{\partial x}\right)^2 \right] \tag{5}$$

and

$c_p$ = specific heat
$k$ = thermal conductivity
$q_i$ = ohmic heating = $(J_x^2 + J_r^2)/\sigma$
$q_r$ = radiation loss
$r$ = radius
$\mu$ = viscosity
$\rho$ = gas density.

Because pressure is assumed to be constant, the last term in equation (4) is zero. The calculation of the thermodynamic properties and equilibrium transport properties will be discussed in section 4.3.

### 4.1.3 Nonequilibrium Energy Equation

Several choices are available for the form of the two energy equations necessary to describe a two-temperature nonequilibrium plasma. In this work, energy equations for the electron energy and the static energy of the whole mixture are used. These equations were chosen because the

form of the energy balance for the whole mixture is the same as that for the equilibrium case [14].

Because the nonequilibrium CAPS code relaxes the LTE assumption, the temperature of the electrons is not necessarily equal to the temperature of the heavy particles. The energy distribution of the heavy particles and the electrons are assumed to be Boltzmann distributions at the heavy particle temperature and electron temperature, respectively. Therefore, the energy in the system must be represented by two energy equations. The equation for the mixture enthalpy, H, is [14]

$$\nabla \cdot \rho \vec{v} H =$$

$$= \nabla \cdot \left[ \frac{k}{C_{p_h}} \nabla H + \left( \rho D - \frac{k}{C_{p_h}} \right) \sum h_i \nabla \alpha_i - k \alpha_e \frac{C_{p_e}}{C_{p_h}} \nabla T_e \right] \qquad (6)$$

$$+ \Phi + q_i - q_r + \vec{v} \cdot \nabla p$$

where

k = thermal conductivity of the mixture

$C_{p_h} = \sum \alpha_i h_i$ = specific heat of heavy particles

where the summation includes the heavy particles.

$C_{pe}$ = specific heat of electrons

D = mixture diffusion coefficient [14]

$\alpha_i$ = concentration of plasma constituent 'i'

$T_e$ = electron temperature.

The last term in equation (6) is zero because of the constant pressure assumption. Equation (6) is one of the energy equations required to represent the two-temperature system modeled in the nonequilibrium CAPS code.

An equation representing the energy in the electron gas is the other equation chosen to represent the energy in the two-temperature system. In this equation, electron conduction, convection, diffusion, and energy transport to the heavy particles through collision [14] balances the electrical Ohmic heating. The form of the equation is taken from Park [23].

$$\nabla \cdot \rho \vec{v} \alpha_e h_e - \nabla \cdot \left[ k_e \nabla T_e + h_e D \nabla \alpha_e \right] - \vec{v} \cdot \nabla p_e = S \qquad (7)$$

where $S = q_{ce} + q_{ch} + q_i - q_r$. The last term on the left-hand side of equation (7) describes the work done by the electron-pressure gradients. This term is zero because of the constant pressure assumption.

"The term $q_{ce}$ represents the transfer of energy between the heavy gas and the electron gas resulting from collisions of electrons with heavy species," [14]

$$q_{ce} = \sum_{i}^{h.p.} 2 n_e \frac{m_e}{m_i} \upsilon_i \frac{3}{2} k \left( T - T_e \right) \qquad (8)$$

where the summation is over the species in the heavy gas. The collision frequency is evaluated from the temperature dependent collision cross-sections for electron-heavy collisions evaluated at the electron temperature using the transport property [routines] described in section 4.3. [14]

Energy transport to the electron gas due to electron participation in chemical reactions is represented by the term, $q_{ch}$, in equation (7). The energy released by a three body recombination reaction with the electron acting as the third body is assumed to be absorbed into the electron gas, raising the electron temperature. Ionization and dissociation due to electron collision is assumed to remove the dissociation or ionization energy from the electron gas, lowering the electron temperature [14].

The electrical energy input to the system, $q_j$, is the same Ohmic heating ($J^2/\sigma$) used in the equilibrium simulation. The thermodynamic and nonequilibrium transport properties are discussed in section 4.3.

### 4.2 Boundary Conditions

The radial gradients of u, H, $h_e$ (in the nonequilibrium case), and p are set equal to zero on the symmetry axis (centerline). A no-slip condition is forced by specifying that the axial velocity is zero at the wall. The axial velocity is calculated from the pressure and the density and is adjusted to ensure the required mass flow. The wall has a specified temperature and is assumed to be catalytic for electron-ion recombination and hydrogen atom recombination. This results in an equilibrium condition at the wall with the gas enthalpy specified by the pressure and the wall temperature. This equilibrium condition at the wall is true in the nonequilibrium plasma as well as the equilibrium plasma [14].

### 4.3 Species

Because the equilibrium CAPS code assumes LTE and chemical equilibrium, species concentrations are a function of pressure and temperature. These concentrations are defined by the Saha equation [6], a form of the law of mass action, which assumes all chemical reactions have equilibrated. The Saha equation cannot be used to obtain nonequilibrium species concentrations since the time scales are too short for chemical reactions to be complete. For this case, finite rate chemical kinetics must be included in the CAPS code model.

For the nonequilibrium CAPS code, the system of governing equations (Section 4.1) are expanded to include three species equations and allow the calculation of systems where ionization of $H$ and the dissociation of $H_2$ are not in equilibrium [14]. The hydrogen system is modeled as a four component system: molecular hydrogen, $H_2$; atomic hydrogen, H; hydrogen ion, $H^+$; and electrons, e. Because the system is electrically neutral, the electrons and hydrogen ions can be represented by the same species conservation equation (this allows the four species

system to be modeled by three species concentration equations). The species conservation equation used in the CAPS code is [14]

$$\nabla \cdot \rho \vec{v} \alpha = \nabla \cdot \rho D \nabla \alpha + S_\alpha \qquad (9)$$

where $\alpha$ is the species under consideration, and $S_\alpha$ is the production of the species by chemical reaction. The source term ($S_\alpha$) is equal to the change in species concentration divided by a chemical time step. This chemical time step is calculated from the mass in the computation cell of interest divided by the mass flux into the cell [14]. The species conservation equations (equation 9) are then solved over the chemical time step using a linearized set of equations for the four hydrogen species [24].

The species production needed in the above calculation are calculated from chemical kinetic reaction rate coefficients. The forward reaction rate coefficients are calculated from the Arrhenius equation [25]

$$k_f = AT^{-n} e^{(E/RT)} \qquad (10)$$

where

A = Arrhenius constant
E = activation energy
R = universal gas constant
T = temperature.

The Arrhenius constant, the activation energy, and the power of the temperature, n, are user input to the computer program. The backward kinetic reaction rate coefficients, $k_b$, are calculated from $k_f$ and the equilibrium constant, $K_p$ [25].

$$k_b = -\frac{k_f}{K_p} \qquad (11)$$

The calculated reaction rates can vary greatly for a chemical reaction depending on the kinetic rate constants used in equation (10). The species concentrations obtained from the computer simulations are extremely sensitive to the calculated rate constants.

Furthermore, a significant amount of the energy is transported between the electrons and the heavy species when an electron acts as the third body in a reactive collision [7]. As a result, the recombination reaction rates can influence the electron to heavy gas temperature ratio, as well as the gas composition. The reaction rates for the hydrogen system used in the computer simulations in this work is presented in Table 1.

### 4.4 Transport Properties

The transport properties for both the equilibrium and nonequilibrium versions of the UTSI cascade arc computer code are calculated using a computer code written by Cho [15] based on the procedures developed by DeVoto [26]. The transport property models used in this reference

are based on the Chapman-Enskog method [27, 28]. The models in Cho's code start with experimental or calculated energy dependent collision cross-sections, calculate the collision integrals based on one of several interaction models and use combinations of the collision integrals to determine the transport properties. Electrical conductivity and electron thermal conductivity depend on collisions between electrons and heavy species in the mixture, while viscosity and heavy gas thermal conductivity depend primarily on collisions between the heavy species [7].

The Cho model makes the following assumptions when used with a two-temperature nonequilibrium plasma model. The fundamental cross-section data describes the interaction of one atom or molecule with another, and depends only upon collision energy and the identity of the colliding pair. The nonequilibrium plasma is described by a two-temperature model where a Maxwellian distribution at a unique electron temperature describes the kinetic energy of the electrons. The electron temperature is used to determine the collision energy for all collisions involving electrons, since the relative velocity of a collision involving an electron is close to the velocity of the electron. The heavy gas temperature is used to determine the collision energy for all other collisions [7].

Radiation transport is calculated using the methods described by Griem [6] that include both line and continuum emission. Energy transport through radiation is modeled as having an optically thin part and an optically thick part. The optically thin radiation is not absorbed back into the plasma gas and is assumed to result in a direct energy loss from the plasma to the constrictor wall of the cascade arc. The optically thick component is absorbed back into the plasma gas and is modeled as a thermal conductivity using the Rosseland approximation [29]. This Rosseland thermal conductivity is fitted as a function of mixture enthalpy, electron concentration, and pressure for a hydrogen plasma in equilibrium. The resulting equation is used in nonequilibrium code [14]. Any error associated with this assumption is assumed to be small because optically thick radiation is very small when compared to the other energy transport mechanisms in hydrogen plasmas at pressures and temperatures realized in the UTSI cascade arc. The Rosseland thermal conductivity is added to the internal thermal conductivity of the heavy species to form an effective thermal conductivity for use in the CAPS code. The Rosseland component is not added to the electron thermal conductivity. Simulations of the UTSI Cascade Arc running on hydrogen have been performed using the CAPS code. Results from these simulations and comparisons with experimental results are presented in Sections 5 and 6.

## 5.0 COMPARISON OF EXPERIMENTAL AND NUMERICAL RESULTS FOR HYDROGEN

The cascade arc was operated with pure hydrogen arcs at 2.0 psi and 6.0 psi and a current of 50 Amps. Several different sets of data were taken at each condition and the data was analyzed using the methods described in Section 3. The spatial FIR smoothing filter used in the Abel inversion algorithm had a cutoff frequency of 4 percent of the Nyquist frequency while the spectral filter had a cut off frequency of 20 percent and 6 percent of Nyquist frequency for the 2 psi and 6 psi cases, respectively. A typical Abel inverted line profile at 6.0 psi and a radius of

1.5 mm and its Voigt fit are shown in Figure 6. This shows the good agreement between experimentally determined profiles and the Voigt lineshapes. The radial profile of the integrated emission data for the 6.0 psi case is shown in Figure 7. The error bars on the emission of plus or minus one standard deviation of the output noise are estimates of the error associated with the Abel inversion. This error was calculated from the variance of the input noise and the spatial bandpass cutoff frequency using a method developed by Smith [30]. Smith shows that "the variance of the output noise is directly proportional to the variance of the input noise and to the bandwidth [of the filter], and inversely proportional to the radial distance from the origin" [30]. As can be seen in Figure 7, the error is inversely proportional to the radius. The error asymptotically approaches infinity as the radius goes to zero. However, when the radius is as little as 20 μm, the standard deviation of the emission has decreased to a few percent of the emission and continues to decrease with radius. The emission has not decreased to zero at 2 mm, the radius of the arc constrictor. A possible explanation for this feature is that the plasma might be slightly bowed into the optical channels leading to the windows. Emission from the plasma core reflected from the constrictor and optical channel walls is also likely to contribute to the emission beyond the 2 mm constrictor radius.

The reaction rates for the hydrogen system used in the computer simulations are shown in Table 1. The "slow" and "fast" rates, presented at the 25th AIAA Plasmadynamics and Lasers Conference[2], have different chemical kinetic rates for the three-body ionization and recombination of hydrogen atoms by electrons. The "U of I" (University of Illinois) rates presented at the 26th AIAA Plasmadynamics and Lasers Conference [1] are the same as the "fast" rates but have a different rate for the dissociation of molecular hydrogen by electrons [31]. The forward reaction rates in Table 1 are given by $k_f = a/T^n \exp(E/RT)$. T is the electron temperature for reactions 3, 3 U of I, 5, 5r, and 5i; and M is any third body. Reaction 5r is the slow recombination rate, and 5i is the slow ionization rate.

Comparisons of the radial distribution of calculated and experimental electron number densities for the 2.0 psi and 6.0 psi cases are presented in Figures 8 and 9, respectively. The same cascade arc data were analyzed using two different Stark broadening models, one that assumes static ions and the other that assumes dynamic ions. The results yielded by each assumption are labeled 'static' and 'dynamic'. The computer simulations were run using the three sets of finite chemical kinetic rates (Table 1). The error bars on the experimental electron number densities (Figures 8 and 9) are plus or minus one standard deviation of the four realizations at each pressure. At 6.0 psi, the nonequilibrium computer simulations underpredict the experimentally determined electron number densities for both the static and dynamic ion assumptions at all radii and for all ionization rates. At 2.0 psi, the experimental electron number densities are underpredicted by all of the simulations when using the static ion assumption. However, the experimental electron number densities are bounded by the simulated nonequilibrium electron number densities for the dynamic ion assumption. While the "dynamic" electron number densities are underpredicted by about an order of magnitude for the "slow" cases, the results for the "fast" case reduce this underprediction to less than a factor of two at 6.0 psi and an overprediction of about 20 percent at 2.0 psi. The "U of I" case gives the best nonequilibrium solution results; it underpredicts the 6.0 psi experimental values by about a factor of two on centerline and matches the centerline experimental value at 2.0 psi. The "U of I" cases also predict the shape of the electron number density profiles better than the solutions using any of

the other chemistry rate sets. The equilibrium simulation predicts that the electron number density becomes negligible at a radius of 1.5 mm while the nonequilibrium simulations predict significant electron densities all the way to the wall. The measured electron densities were also significant all the way to the wall verifying that the cascade arc plasmas are in nonequilibrium.

Figures 10 and 11 show comparisons of the radial distribution of calculated and experimental electron temperatures for the 2.0 psi and 6.0 psi cases, respectively. Only the "U of I" nonequilibrium solutions are presented in these plots for the sake of brevity. The computer simulations overpredict the experimental centerline temperatures by approximately 60 percent for the 2.0 psi case and match the experiment (within experimental error) for the 6.0 psi case. The measured temperature profiles do not match any of simulation temperature distributions. The negative temperature gradient at the constrictor wall and the 50 percent error of the experimental temperature distributions make these preliminary data questionable. The error bars on the experimental data are plus or minus one standard deviation calculated from the uncertainty associated with the slope of the line in the Boltzmann plot (the Boltzmann plot of a 6 psi hydrogen arc is shown in Figure 12). The relatively large error in temperature results from poor fits through the four data points in the Boltzmann plots.

Table 2 is a comparison of the experimental and numerical electric field for the 2.0 psi and 6.0 psi cases. The experimental electric fields were determined by finding the slope of the best fit line through the measured potentials of the cascade plates. The electric fields from the equilibrium simulations overpredict the experimentally determined values by 33 percent for the 2.0 psi case and 10 percent for the 6.0 psi case. These overpredictions increase to 180 percent and 51 percent for the "slow" nonequilibrium simulations at 2.0 psi and 6.0 psi, respectively. The electric field for the "fast" nonequilibrium simulations overpredicts the experiment by 17 percent for 2.0 psi and agrees with the value for 6.0 psi. The "U of I" nonequilibrium simulations best predict the electric field, underprdicting the value for the 2.0 psi case by less than 5 percent and matching the value for the 6.0 psi case. It is evident that the chemical kinetic rates have a large impact on the electric field realized in the nonequilibrium computer simulations.

## 6.0 RESULTS FOR HYDROGEN/NITROGEN PLASMAS

The cascade arc was also operated on simulated ammonia and hydrazine at 2.0, 6.0, and 10.0 psi and 50 Amps. The radial distribution of experimental electron number densities for simulated ammonia and simulated hydrazine are shown in Figures 13 and 14, respectively. These data show an increase in electron density with pressure, and a very slight increase in electron density for the hydrazine over the ammonia. An interesting feature of the profiles is the positive slope of the curve close to the wall of the arc channel at 2 mm. This feature can be explained by a combination of two factors, both magnified by a low signal level at these larger radii. First, some of the light from the broader lines near the arc center can reflect off of the optical channel walls so that it appears to be originating closer to the wall of the constrictor. This reflected light effectively broadens the thinner and weaker line emission near the constrictor wall. Second, it is very difficult to determine the exact magnitude of the continuum. A small increase in the background level can cause artificial broadening in the Abel inversion technique. Table 3 shows

a comparison of experimentally determined electric fields for the hydrogen and hydrogen/nitrogen mixtures. The electric field increases with pressure and decreases as more nitrogen is added.

## 7.0 DISCUSSION OF RESULTS

The comparisons of the radial distributions of electron number density presented in Section 5 show discrepancies ranging from as low as 50 percent to as high as 1.5 orders of magnitude. The magnitude of the discrepancy depends on which chemical kinetic rates were utilized in the CAPS code simulations and whether the static ion or dynamic ion assumption was utilized in the Stark broadening theory implemented in the data analysis. The results make it apparent that the dynamic ion assumption is best suited for analysis of the hydrogen plasmas realized in the cascade arc. Not only are the discrepancies between the experimental and simulated electron number density distributions significantly reduced from the static ion results, the measured line emission profiles are largely Lorentzian (as predicted by dynamic ion Stark broadening theory) [32]. Unfortunately, discrepancies in electron number densities do exist between the computer simulation results and the "dynamic ion" experimental results. These discrepancies result from either error in the CAPS code simulations, experimental error, or a combination of the two.

Good agreement between the simulated axial electric fields was realized with the "U of I" kinetics set. Determination of the experimental axial electric field from the easily measured potentials of cascade arc constrictor plates is a very simple procedure that leads to a high degree of confidence in the experimental electric fields. Because the "U of I" rate set leads to solutions that are in good agreement with the measured axial electric fields, confidence in this chemical kinetic rate set is high. However, differences between the simulated and the experimental electron number densities must be investigated.

Obviously, incorrect finite rate chemical kinetics and nonequilibrium transport properties could lead to the discrepancies in the electron number density distributions. Parametric studies have been run to determine the affects of artificially changing nonequilibrium transport properties and finite rate chemical kinetics. Any of these changes that led to a reduction in the discrepancies in the electron number density profiles created large discrepancies in the axial electric fields which were originally in good agreement. Therefore, it seems unlikely that changes in the finite rate chemical kinetics and the nonequilibrium transport properties could resolve the discrepancies in the electron number densities without adversely affecting the simulated electric field. All of the CAPS code solutions are well converged, and the computation grid was found not to influence the simulation results. Therefore, the CAPS code simulations cannot account for the discrepancies in the electron number densities, and uncertainties in the experimental number densities must account for a substantial portion of the discrepancies realized.

The uncertainty associated with the electron number densities determined from the dynamic ion Stark broadening theory does have considerable uncertainty associated with it. The experimental electron number densities (dynamic ion) are determined by fitting Voigt profiles to the radial distribution of $H_\alpha$ emission line profiles and correlating the width of the Voigt profile's Lorentzian component to the width of a theoretical, "dynamic" Stark broadened line. Any error

associated with this process is comprised of uncertainty associated with the Voigt profile fitting routine, uncertainty in the theoretical values of the "dynamic" Stark broadened emission line widths, and the quality of the emission line data being analyzed. The uncertainty in the theoretical values for the "dynamic" Stark broadened emission line widths was estimated by Oza et. al. [12] to be approximately 10 percent. This error contribution is significant, but cannot account for all of the discrepancies in the electron number density comparisons.

As mentioned in Section 5, the Voigt profile fitting routine results in excellent theoretical fits to the experimental emission profiles. However, the sensitivity of the electron number densities to the fitted Voigt profiles was not known *a priori*, and needed to be investigated. By utilizing the radial distributions of heavy particle temperature and electron number density from the "U of I" Caps code simulations, radial distributions of simulated Voigt profiles were constructed. These profiles were fitted to the experimental emission profiles to get a feel for the sensitivity of the electron densities to the fitted Voigt profiles. The results of this study are shown if Figures 15, 16, 18, and 19. Each of these figures contains an experimental emission line profile and three fitted Voigt profiles. The Voigt profiles labeled "Sim. T, Ne profile" are simulated profiles constructed using the simulated (U of I) temperatures (Gaussian component) and electron number densities (Lorentzian component). The profiles labeled "Sim. Ne profile" are simulated Voigt profiles constructed using the electron number densities from the "U of I" simulations to determine the Lorentzian components of the Voigt profiles; the downhill Simplex routine finds the best Gaussian (Doppler) components. The measured emission profiles are largely Lorentzian and the fitted Voigt profiles are relatively insensitive to their Gaussian components. This leads to very minor differences between the profiles labeled "Sim. T, Ne profile" and the profiles labeled "Sim. Ne profile". The Voigt profiles labeled "Best fit Voigt" were obtained from the downhill simplex fitting routine to determine both the Lorentzian and Gaussian components of the profile. These are the Voigt profiles from which the experimental electron number densities are obtained.

Figures 15 and 16 contain comparisons of the fitted Voigt profiles to the $H_\alpha$ emission lines from a 50 Amp hydrogen arc at 6.0 psi at radii of 0.03 mm and 1.5 mm, respectively. The emission line data at 0.03 mm is quite noisy and leads to relatively poor fits. At this small radius, the simulated profiles are broader than the "Best fit Voigt" profiles. However, the simulated profiles appear to represent the noisy experimental data as well as the "Best fit Voigt" profile does. At a radius of 1.5 mm, the simulated profiles and the "Best fit Voigt" profile are virtually indistinguishable and represent the experimental results equally well. In an attempt to quantify the error associated with the "Best fit Voigt" profile and the simulated Voigt profiles, the sum of the square of the difference between the experimental emission profile and each of the fitted Voigt profiles over all spectral locations were determined. This calculation was repeated for every radial position. The results of this analysis are shown in Figure 17. Because the "Sim. T, Ne" and the "Sim. Ne" profiles are so similar, only the "Sim. Ne" case is shown in the figure. The "Best fit Voigt" profiles generally have smaller error, and the error in the simulated profile fits are greatest near the centerline where the largest discrepancies in the electron number density comparisons are realized for the 6.0 psi case. However, not only is the maximum error in the simulated profile fits less than a few percent of the total line emission at the same location, the error due to Abel inversion was not taken into account in the downhill Simplex fitting routine. The Abel inversion error is largest on centerline and would significantly reduce the error in the

simulated Voigt fits in this region. Therefore, the simulated Voigt profiles calculated from the "U of I" simulation results are believed to adequately predict the experimental emission profiles. Thus, the radial distribution of electron number density from the "U of I" simulation at 6.0 psi predicts the experimental electron densities much better than indicated in Figure 9. The large sensitivity of the electron number density to the Voigt fitting routine leads to experimental uncertainty that accounts for a large portion of the discrepancy between the simulated and experimental electron densities at 6.0 psi.

The analysis of the sensitivity of the electron number densities to the Voigt profile fits was repeated for the 2.0 psi hydrogen arc data. Figures 18 and 19 contain comparisons of the fitted Voigt profiles to the $H_\alpha$ emission lines from a 50 Amp hydrogen arc at 2.0 psi at radii of 0.03 mm and 1.5 mm, respectively. Only slight differences exist between the "Best fit Voigt" and simulated Voigt profiles at a radius of 0.03 mm, all of which reasonably predict the experimental emission profile (Figure 18). This is expected because the "U of I" simulation correctly predicts the experimentally determined electron number densities near the centerline for the 2.0 psi case (see Figure 8). For radii beyond about 1.0 mm, the simulated Voigt profiles do not predict the experimental emission profiles nearly as well as the "Best fit Voigt" profiles. Figure 6.18 shows the Voigt profile fits to the measured emission line at a radius of 1.5 mm. This radius corresponds to the largest discrepancy in the electron number density comparisons for the 2.0 psi case (see Figure 8). Therefore, the fits of the simulated Voigt profiles at the 1.5 mm radius are worse than the fits at any other radius. At the 1.5 mm radius the simulated profiles are broader than the measured emission line indicating larger simulated electron number densities than realized in the experiment. Figure 20 shows the radial distribution of the error in the simulated and "Best fit Voigt" profiles for the 2.0 psi case. As was seen for the 6.0 psi case, the "Best fit Voigt" profiles generally have smaller error. But, unlike the 6.0 psi case, the error in the simulated profile fits at 2.0 psi are greatest near a radius of 1.5 mm where the largest discrepancy in the electron number density comparison is realized. The largest Voigt fitting error is, however, less than a few percent of the line emission at that same radius. The results of the above analysis indicates that, even though the sensitivity of the electron number density to the Voigt fitting routine is quite significant, this sensitivity cannot account for all of the discrepancies in the electron number density comparisons for the 2.0 psi case as it did for the 6.0 psi case.

In addition to the sensitivity of the electron number densities to the Voigt profile fitting routine, the quality of the experimental emission profiles affects the uncertainty associated with the experimentally determined electron number densities. The cascade arc emission line data is potentially degraded by three sources: self absorption of the $H_\alpha$ line, high frequency noise, and low intensity signal.

Any self absorption of the $H_\alpha$ line would lower the peak of the emission line and effectively broaden the line shape. A characteristic feature of a self absorbed line is a dip in the emission at the spectral center of the line. None of the $H_\alpha$ line data collected had this feature; therefore, the line is not strongly self absorbed. However, weaker self absorption will tend to flatten the peak of the emission line, instead of creating a dip. This situation will also broaden the line, although to a lesser degree. To determine the extent of self absorption of the $H_\alpha$ line in the cascade arc

data, the optical thickness, $\tau_\nu$, of the plasma was calculated. The optical thickness of a plasma is given by [33]:

$$\tau_\nu = \kappa'_\nu L \qquad (12)$$

where

$\kappa'_\nu$ = the absorption coefficient at wavelength $\nu$,

L = the characteristic length of the plasma.

The absorption coefficient of the $H_\alpha$ line is calculated using the methods given in Boulos [33]. If the plasma is optically thick ($\tau_\nu >> 1$), self absorption is significant. If the plasma is optically thin ($\tau_\nu << 1$), line emission passes through the plasma without being absorbed. The optical thickness for the $H_\alpha$ line in the 6.0 psi hydrogen arc was calculated to be approximately 0.01. Therefore, this hydrogen plasma is relatively thin for the $H_\alpha$ line, and self absorption should be fairly insignificant. This same result was obtained by other researchers for a hydrogen plasma, under similar conditions but generated in a different device, where self absorption was both calculated and experimentally demonstrated to be insignificant [34]. Because plasmas are more optically thick at higher pressures, the optical thickness of the 2.0 psi hydrogen plasma in the cascade arc is also optically thin. Therefore, self absorption is not believed to significantly degrade the $H_\alpha$ line emission data.

The same is not true for the effects of high frequency noise and low signal in the $H_\alpha$ line emission data. The high frequency noise is filtered during Abel inversion, and the associated error was discussed previously. The low intensity signal results in small signal to background noise ratios across the entire arc. The spectrally resolved signal to noise ratios of the unaltered intensity data of the $H_\alpha$ line at radii near the centerline and approximately 1.5 mm are shown in Figures 21 and 22 for the 6.0 psi and 2.0 psi cases, respectively. The maximum signal to noise ratios occur near the center of the arc and have values less than 2.4 for both pressures. As the edge of the arc is approached, the signal decreases significantly. The signal also decreases as one moves spectrally away from the spectral center of the $H_\alpha$ line. Therefore, the intensity signal in the wings is quite poor. This effect is more profound for the 2.0 psi arc at larger radii. Because of long exposure times used in the data acquisition and the physical limitations of the 2-D OMA/image intensifier combination, significantly larger signal to noise ratios were unobtainable. The low signal of the $H_\alpha$ line intensity amplifies the uncertainty in the Voigt line fitting discussed above.

As seen in Figures 21 and 22, the width of the $H_\alpha$ line is much smaller for the arc at 2.0 psi than the arc at 6.0 psi. In the Abel inversion routine, the emission lines are transformed into the Fourier domain. In the Fourier domain, the thinner emission lines at 2.0 psi are comprised of higher frequencies than the wider emission lines at 6.0 psi. The highest frequency components add definition to the lineshape--especially in the wings. Unfortunately, the experimental emission data has high frequency noise that interferes with the details of the lineshape. To some degree, the high frequency noise and the high frequency components of the line become indistinguishable. The high frequency noise has to be filtered out for the fitting routines to work properly. This results in the removal of detail in the lineshape--removing definition from the wing and effectively narrowing the line. Though this effect is relatively insignificant for the broad lines realized at 6.0 psi, it has great impact on the much narrower lines at 2.0 psi,

especially at larger radii where the intensity is very low. Figure 23 shows a comparison of the signal to noise ratio of the spectral $H_\alpha$ line profiles for the 2.0 psi and 6.0 psi cases at a radius of about 1.5 mm. This plot emphasizes the narrowness of the 2.0 psi lineshape and the low intensity in the wings.

The error associated with the experimental data and the data analysis introduces a lot of uncertainty into the radial distributions of electron number density. Most of this uncertainty is attributed to three things: the sensitivity of the electron densities to the Voigt fitting routine; the 10 percent uncertainty associated with the correlation of the dynamic ion Stark broadened line width to the electron number density; and the low intensity signal from the $H_\alpha$ emission line. Although it has not been quantified, the total uncertainty in the measured electron number densities makes it very difficult to claim that the electron densities predicted by the "U of I" CAPS code simulations are wrong.

## 8.0 CONCLUSIONS

Nonequilibrium plasma conditions of 50 Amp hydrogen arcs at 2.0 and 6.0 psi have been measured and compared with computer simulations using the UTSI CAPS code. The simulations have been run with a wide range of chemical kinetics. The simulated plasma conditions were found to be extremely sensitive to the kinetics. The predicted nonequilibrium electron number densities underpredicted the experimental values (using the dynamic ion assumption) by as much as an order of magnitude and overpredicted the experimental values by as much as a factor of two, depending on the kinetics model utilized and the arc pressure. The peak electron densities were consistently overpredicted by the equilibrium solutions. The experimental electric fields were bounded by the nonequilibrium computer simulation results by using different finite rate chemical kinetic rates. The "U of I" finite rate chemical kinetic model matches the experimental electric field and best predicts the distribution of electron number densities. Even though the "U of I" rates do not match the measured electron densities, the uncertainty associated with the experimental electron number densities makes it very difficult to claim that the electron densities predicted by the "U of I" simulations are incorrect. The "U of I" chemical kinetic rate set, therefore, is believed to be the best finite rate chemical kinetics set tested for hydrogen. In addition to the measured distributions of electron number densities, Boltzmann plots have been used to determine a rough estimate for the radial distribution of plasma electron temperature. These preliminary experimental temperature data are overpredicted by the simulations by as much as 2.5 times.

Electron number density profiles for simulated ammonia and simulated hydrazine have been obtained for 50 Amp arcs at 2 psi, 6 psi, and 10 psi. The measured electric field was found to vary directly with pressure and inversely with nitrogen content. The measured electron number density followed opposite trends. A hydrogen/nitrogen mixture version of the CAPS code is currently being developed to provide comparisons with the experimental mixture data.

## ACKNOWLEDGMENTS

This work was supported by the Air Force Office of Scientific Research under contract #F49620-97-1-0223 and the National Science Foundation under NSF Grant # CTS-9512489.

## REFERENCES

1. T. Megli, H. Krier, and R.Burton, "A Plasmadynamics Model for Nonequilibrium Processes in N2/H2 Arcjets," AIAA 95-1961, 26th AIAA Plasmadynamics and Lasers Conference, San Diego, CA, June 19-22, 1995.

2. D. Keefer, D. Burtner, T. Moeller, and R. Rhodes, "Multiplexed Laser Induced Fluorescence and Non-equilibrium Processes in Arcjets," AIAA 94-2656, 25th AIAA Plasmadynamic and Lasers Conference, Colorado Springs, CO, June, 1994.

3. S. Miller, and M. Martinez-Sanchez, "Nonequilibrium Numerical Simulation of Radiation Cooled Arcjets," IEPC-93-218, *Proceedings of the 23rd International Electric Propulsion Conference*, Vol. 3: 2032-2050, Published at The Ohio State University, Columbus OH, 1993.

4. G. W. Butler, B. A .Kashiwa, and D. Q. King, "Numerical Modeling of Arcjet Performance," AIAA 90-1474, AIAA 21st Fluid Dynamics, Plasma Dynamics and Lasers Conference, Seattle, WA, June, 1990.

5. W. L. Wiese, D. R. Paquette, and J. E. Solarski, "Profiles of Stark-Broadened Balmer Lines in a Hydrogen Plasma," *Phys. Rev.*, 129:1225-1232, February, 1963.

6. H. Griem, *Plasma Spectroscopy*, McGraw-Hill, 1964.

7. T. Moeller, D. Keefer, and R. Rhodes, "Cascade Arc Studies of Nonequilibrium Hydrogen Plasmas," AIAA 96-3294, 32nd AIAA/ASME/SAE/ASEE Joint Propulsion Conference, Lake Buena Vista, FL, July 1-3, 1996.

8. R. Gonzalez, and P. Wintz, *Digital Image Processing*, Addison-Wesley Publishing, Ontario, 1977, pp. 199-209.

9. T. Moeller, D. Keefer, and R. Rhodes, " Studies of Nonequilibrium Hydrogen/Nitrogen Plasmas using a Cascade Arc," AIP Conference Proceedings 387, p. 317, The Space Technology and Applications International Forum (STAIF-97), Albuquerque, NM, Jan. 1997.

10. L. M. Smith, D. Keefer, and S.I. Sudharsanan, "Abel Inversion Using Transform Techniques," *J. Quant. Spectrosc. Radiat. Transfer*, 39:367-373, 1988.

11. W.H. Press, S.A. Teukolsky, W.T. Vetterling, and B.P. Flannery, *Numerical Recipes in FORTRAN*, 2nd ed. Cambridge University Press, Cambridge, 1992.

12. D.H. Oza, R.L. Greene, and D.E. Kelleher, "Collisional Broadening of the Balmer-α Transition of H and $He^+$ in Plasmas," *Physical Review A*, Vol. 37, No. 2, Jan. 1988.

13. T. Moeller, D. Keefer, and R. Rhodes, "Nonequilibrium Hydrogen/Nitrogen Plasmas Studies Using a Cascade Arc," IEPC 97-063, 25th International Electric Propulsion Conference, Cleveland, OH, August, 1997.

14. R. Rhodes, and D. Keefer, "Non-equilibrium Modeling of Hydrogen Arcjet Thrusters," IEPC-93-217, *Proceedings of The 23rd International Electric Propulsion Conference*, Vol. 3: 2020-2031, Published at The Ohio State University, Columbus, OH, 1993.

15. K. Y. Cho, "Non-Equilibrium Thermodynamic Models and Applications to Hydrogen Plasmas," Ph.D. Thesis, Georgia Institute of Technology, March 1988.

16. A. D. Gosman and W. M. Pun, "Calculation of Recirculation Flows," Report No. HTS/74/12, Dept. of Mechanical Engineering, Imperial College, London, 1974.

17. C. M. Rhie, "A Pressure Based Navier-Stokes Solver," AIAA paper 86-0207, 24th AIAA Aerospace Sciences Meeting," Reno, Nevada, January 1986.

18. T. M. Moeller, "Comparison of Experimental and Numerical Results for Radiation Cooled and Water Cooled Hydrogen Arcjets," *Proceedings of the 23rd International Electric Propulsion Conference*, Vol. 3: 1979-1988, Published at The Ohio State University, Columbus OH, 1993.

19. T.M. Moeller, "Comparison of Experimental and Numerical Results for Radiation Cooled and Water Cooled Hydrogen Arcjets," Masters Thesis, University of Tennessee Space Institute, 1993.

20. R. P. Rhodes, and D. Keefer, "Numerical Modeling of a Radio Frequency Plasma in Argon," *AIAA Journal*, Vol. 27, No. 12, December 1989, pp. 1779-1784.

21. R. Rhodes and D. Keefer, "Comparison of Model Calculations with Experimental Data from Hydrogen Arcjets," Paper 91-111, 22nd International Electric Propulsion Conference, Viareggio, Italy, October, 1991.

22. D. Keefer, D. Burtner, T. Moeller, and R. Rhodes, "Multiplexed Laser Induced Fluorescence and Non-equilibrium Processes in Arcjets," AIAA 94-2656, 25th AIAA Plasmadynamic and Lasers Conference, Colorado Springs, CO, June, 1994.

23. C. Park, *Non-equilibrium Hypersonic Aerothermodynamics*, John Wiley & Sons, New York, 1990.

24. R. R. Mikatarian, C.J. Kau, and H.S. Pergament, "A Fast Computer Program for Nonequilibrium Rocket Plume Predictions," AeroChem TP-282, August 1972.

25. K. K. Kuo, *Principles of Combustion*, John Wiley & Sons, New York, 1986.

26. R. S. DeVoto, "The Transport Properties of a Partially Ionized Monatomic Gas," Ph.D. Thesis, Stanford University, 1965.

27. S. Chapman and T.G. Cowling, *Mathematical Theory of Non Uniform Gases*, 3rd ed., Cambridge University Press, New York, 1970.

28. J.O. Hirschfelder, C.F. Curtiss, and R.B. Bird, *Molecular Theory of Gases and Liquids*, John Wiley & Sons, 1964.

29. R. Siegal, and J.R. Howell, *Thermal Radiation Heat Transfer*, 3rd ed., Hemisphere Publishing Corp., Washington, D.C., 1992.

30. L.M. Smith, "Nonstationary Noise Effects in the Abel Inversion," *IEEE Transactions on Information Theory*, Vol. 34, N0. 1, pp. 158-161, Jan. 1988.

31. Janev, et al, *Elementary Processes in Hydrogen Helium Plasmas*, Springer-Verlag, New York, 1987.

32. D.H. Oza, R.L. Greene, and D.E. Kelleher, "Dependence of the half width of plasma-broadened hydrogen lines on reduced mass, temperature, and density," *Physical Review A*, Vol. 38, No. 5, September 1988.

33. M.I. Boulos, P. Fauchais, E. Pfender, *Thermal Plasmas Fundamentals and Applications*, Vol. 1, Plenum Press, New York 1994.

34. C. Fleuier, G. Coulaaud, P. Ranson, "Ion-motion effect in the Stark profiles of Hα and Hβ," *Phsyical Review A*, Vol. 21, No. 3.

Table 1. Reaction Rates for Hydrogen.

| | Reaction | a | n | E |
|---|---|---|---|---|
| 1 | $H + H + M \leftrightarrow H_2 + M$ | 6.40e+17 | 1.0 | 0. |
| 2 | $H^+ + e + M \leftrightarrow H + M$ | 5.26e+26 | 2.5 | 0. |
| 3<br>U of I | U of I<br>$H_2 + e \rightarrow H + H + e$ | 1.87e-3 | -3.73 | 0. |
| 3 | $H_2 + e \rightarrow H + H + e$ | 1.91e+11 | -1.0 | -203. |
| 4 | $H^+ + e \rightarrow H + h\nu$ | 3.77e+13 | 0.58 | 0. |
| 5 | fast rates<br>$H^+ + e + e \leftrightarrow H + e$ | 7.08e+39 | 4.5 | 0. |
| 5r | slow rates<br>$H^+ + e + e \rightarrow H + e$ | 2.19e+41 | 5.06 | 0. |
| 5i | $H + e \rightarrow H^+ + e + e$ | 1.81e+14 | 0. | -244750 |

Table 2. Comparison of Experimentally Determined Electric Field (V/cm) with UTSI Cascade Arc Plasma Simulation (CAPS) Code Values.

| | Equilibrium Simulation | "Slow" Non-Equilibrium | "Fast" Non-Equilibrium | "U of I" Non-Equilibrium | Experiment |
|---|---|---|---|---|---|
| Case 1: 2.0 psi | 46.4 | 95.7 | 42.0 | 33.4 | $36.0 \pm 1.2$ |
| Case 2: 6.o psi | 46.3 | 64.9 | 43.9 | 44.1 | $44.2 \pm 1.2$ |

Table 3. Experimentally Determined Electric Field (V/cm) for Hydrogen and Hydrogen/Nitrogen Mixtures.

| | Hydrogen | Simulated Ammonia | Simulated Hydrazine |
|---|---|---|---|
| Case 1: 2.0 psi | 36.0 ± 1.2 | 26.4 ± 0.7 | 26.2 ± 0.8 |
| Case 2: 6.0 psi | 44.2 ± 1.2 | 38.8 ± 1.1 | 35.1 ± 0.9 |

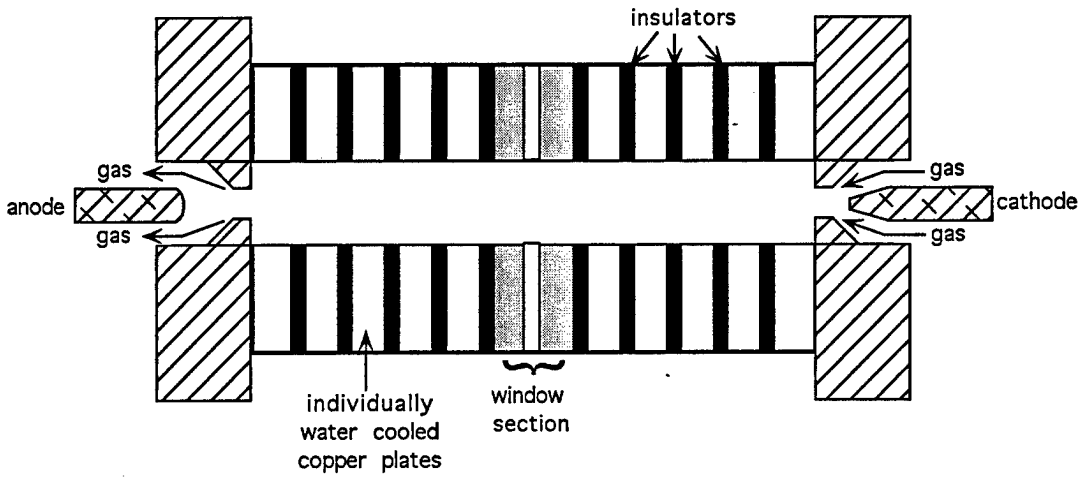


Figure 1. Cascade Arc Assembly.

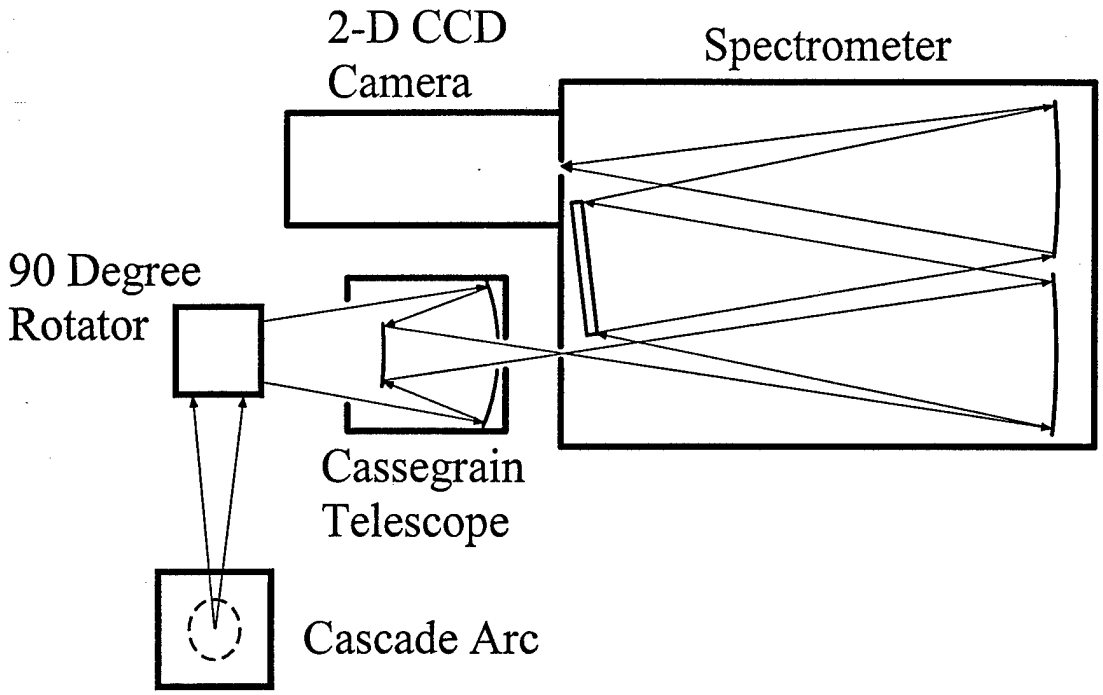


Figure 2. Schematic of the optical setup.

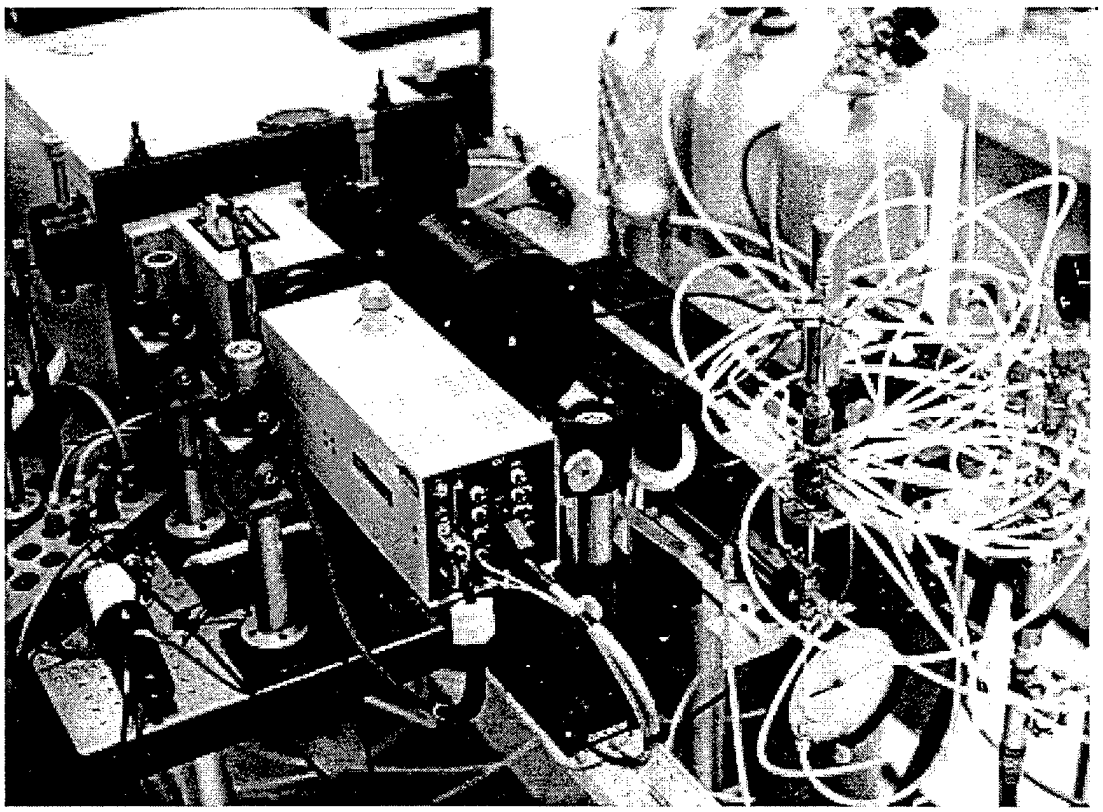

Figure 3. Picture of the UTSI Cascade Arc Facility and external optics.

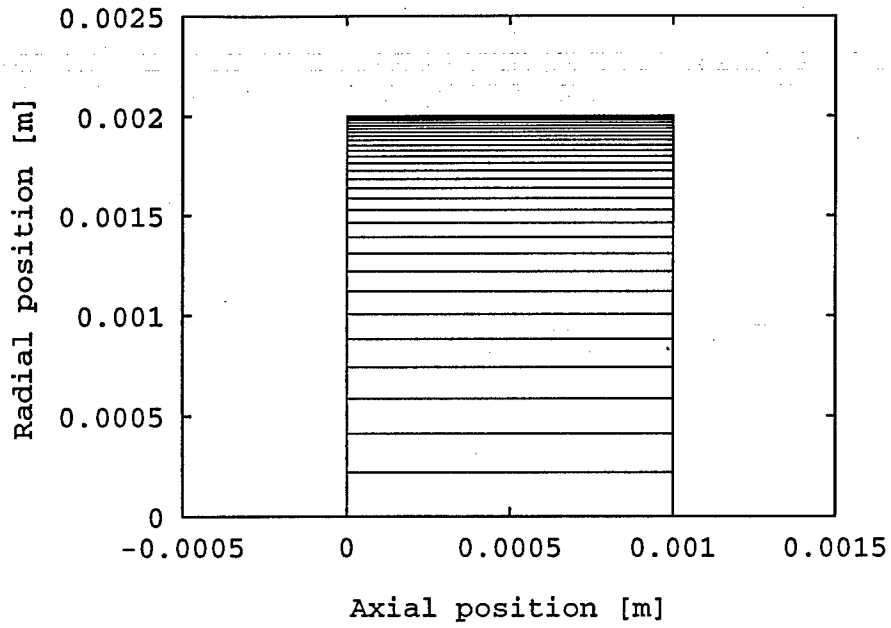


Figure 4 Computation grid (in spatial coordinates) used in the CAPS code simulations.

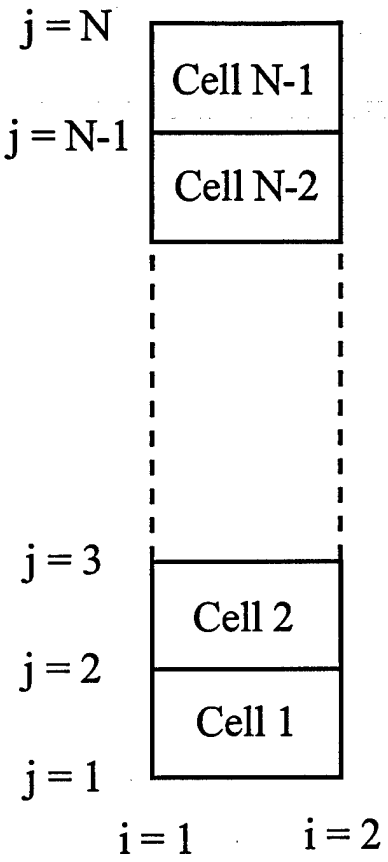


Figure 5 Computation cells surrounding points in a transformed computation grid. There are N grid points and N-1 cells in the radial direction.

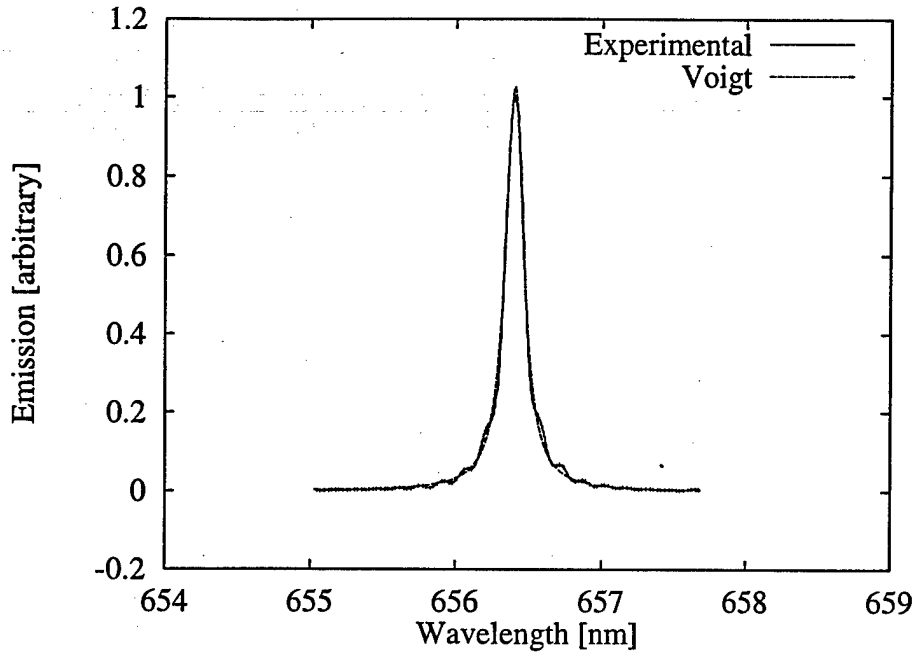


Figure 6. Measured and Fitted Theoretical Voigt Lineshapes of $H_\alpha$ Line in a 50 Amp Hydrogen Arc at 6.0 psi at a Radius of 1.5 mm.

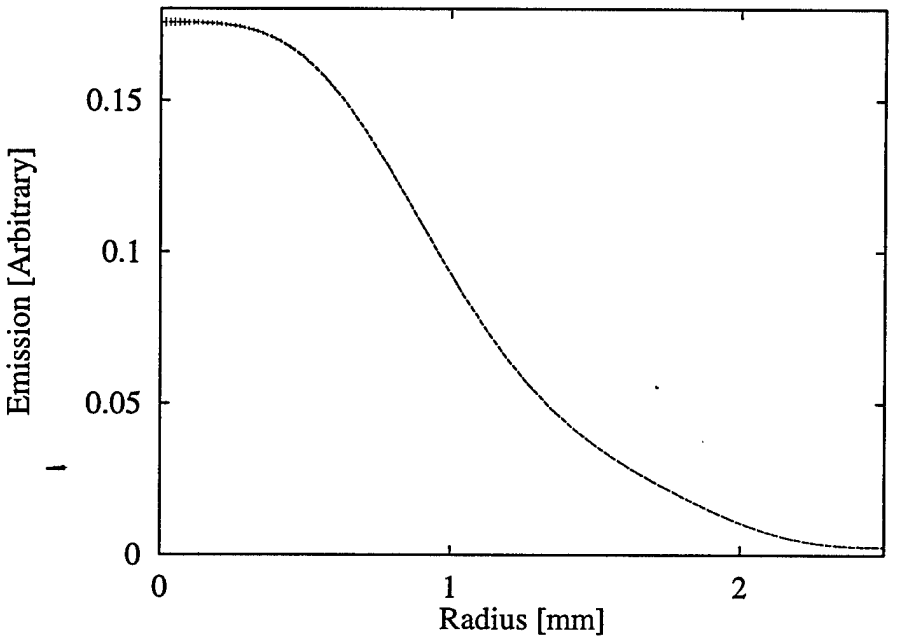


Figure 7. Radial profile of integrated emission for a 50 Amp hydrogen arc at 6 psi.

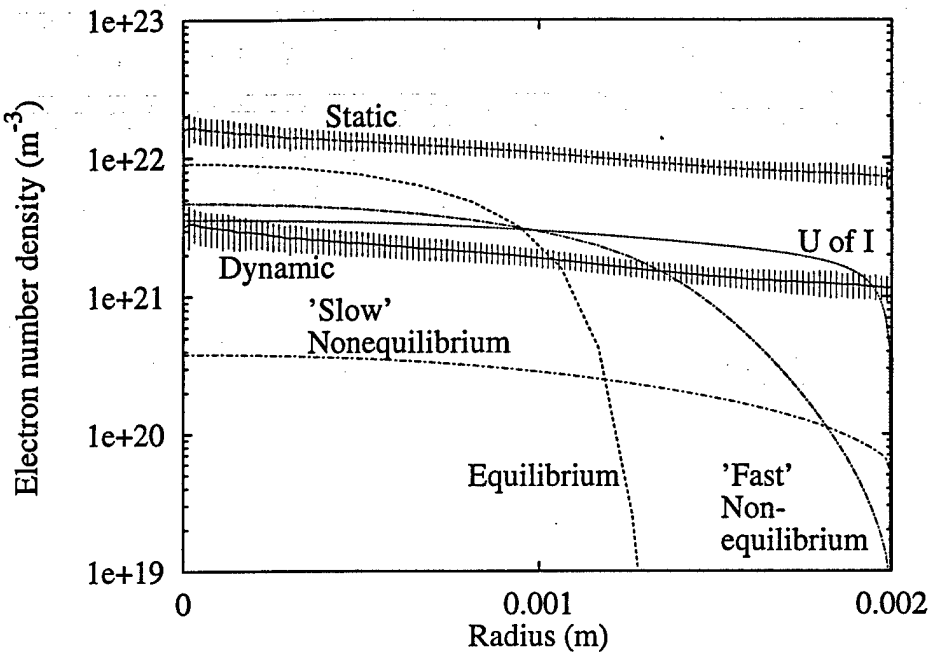


Figure 8. Comparison of Experimental and Numerical Radial Distributions of Electron Number Density in a 50 Amp Hydrogen Arc at 2.0 psi. "Fast" and "slow" represent nonequilibrium computer simulations using two different chemical kinetic rates for the ionization of hydrogen due to electrons. "U of I" indicates a finite rate solution using a different rate for the dissociation of hydrogen by electrons.

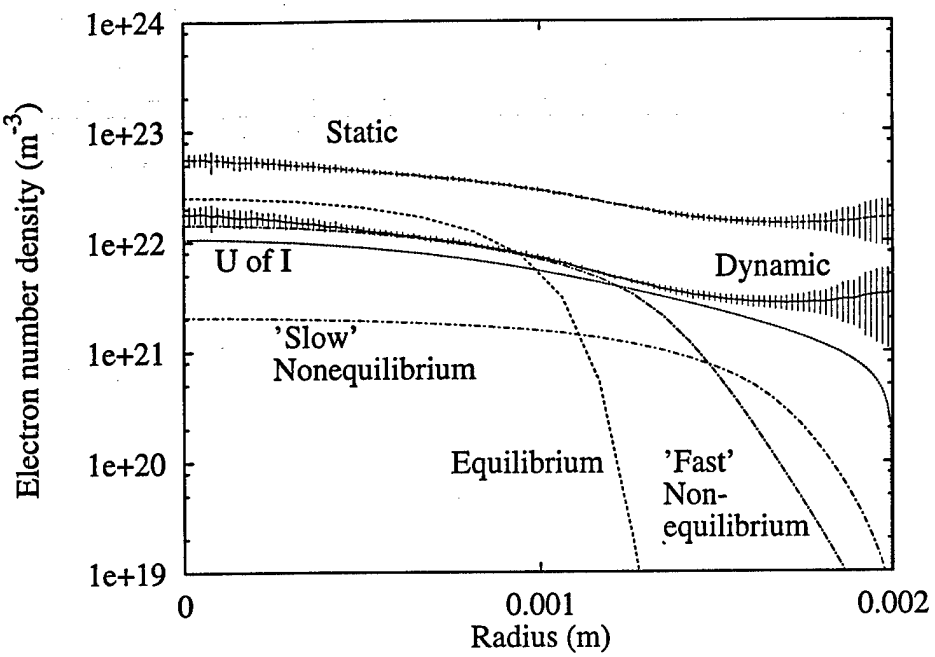


Figure 9. Comparison of Experimental and Numerical Radial Distributions of Electron Number Density in a 50 Amp Hydrogen Arc at 6.0 psi. "Fast" and "slow" represent nonequilibrium computer simulations using two different chemical kinetic rates for the ionization of hydrogen due to electrons. "U of I" indicates a finite rate solution using a different rate for the dissociation of hydrogen by electrons.

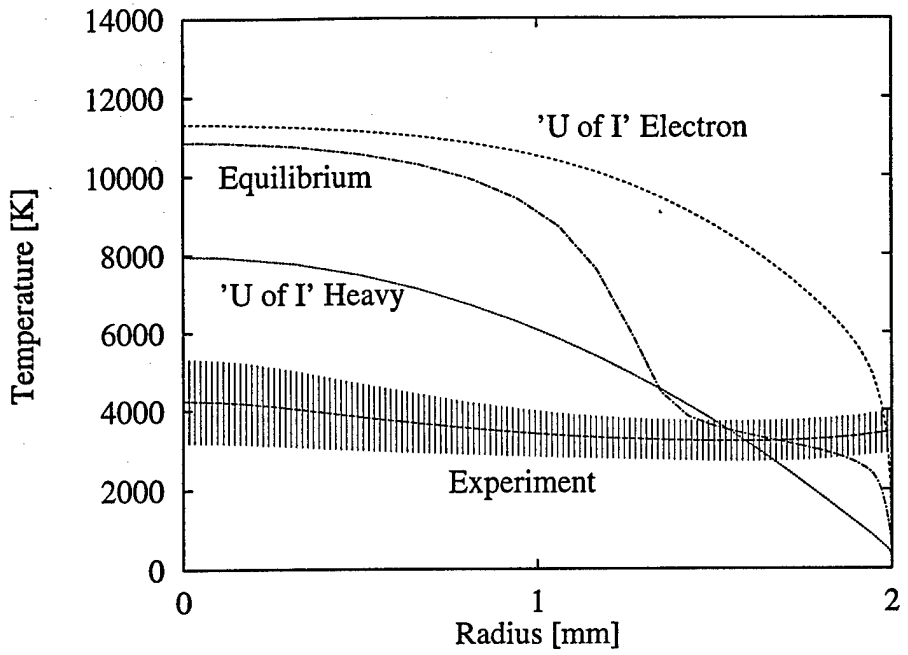


Figure 10. Comparison of Experimental and Numerical Radial Distributions of the Plasma Temperature in a 50 Amp Hydrogen Arc at 2.0 psi. "U of I" indicates a finite rate solution using "U of I" kinetics.

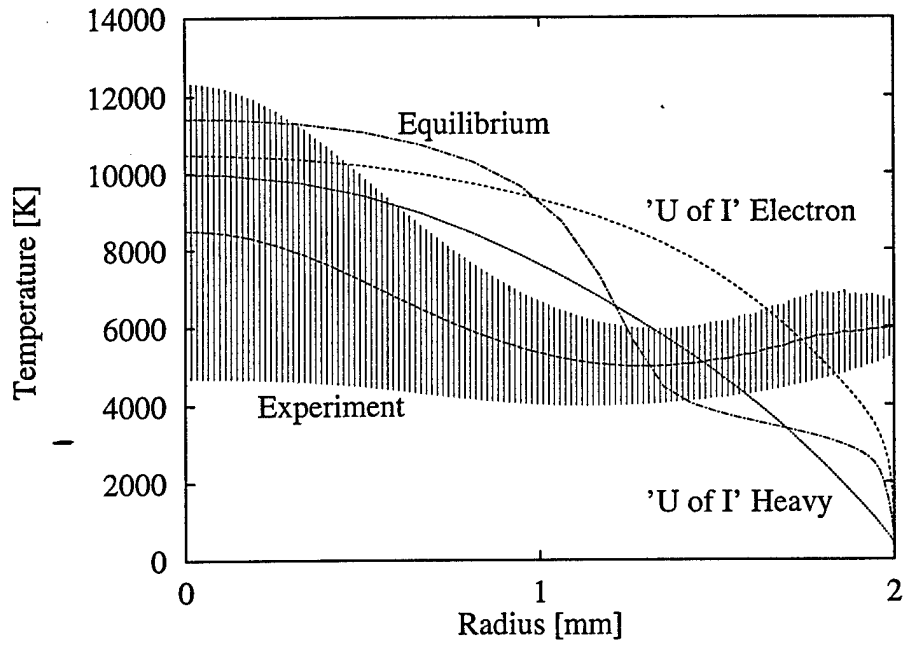


Figure 11. Comparison of Experimental and Numerical Radial Distributions of the Plasma Temperature in a 50 Amp Hydrogen Arc at 6.0 psi. "U of I" indicates a finite rate solution using "U of I" kinetics.

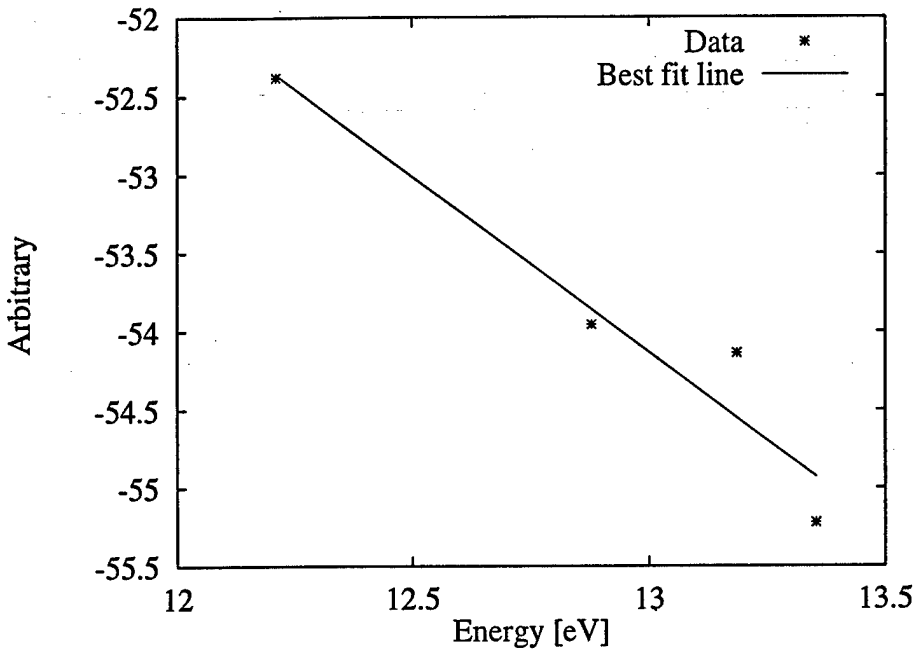


Figure 12. Boltzmann Plot Using the $H_\alpha$, $H_\beta$, $H_\gamma$, and $H_\delta$ Lines in a 50 Amp Hydrogen Arc at 6.0 psi at a Radius of 1.5 mm.

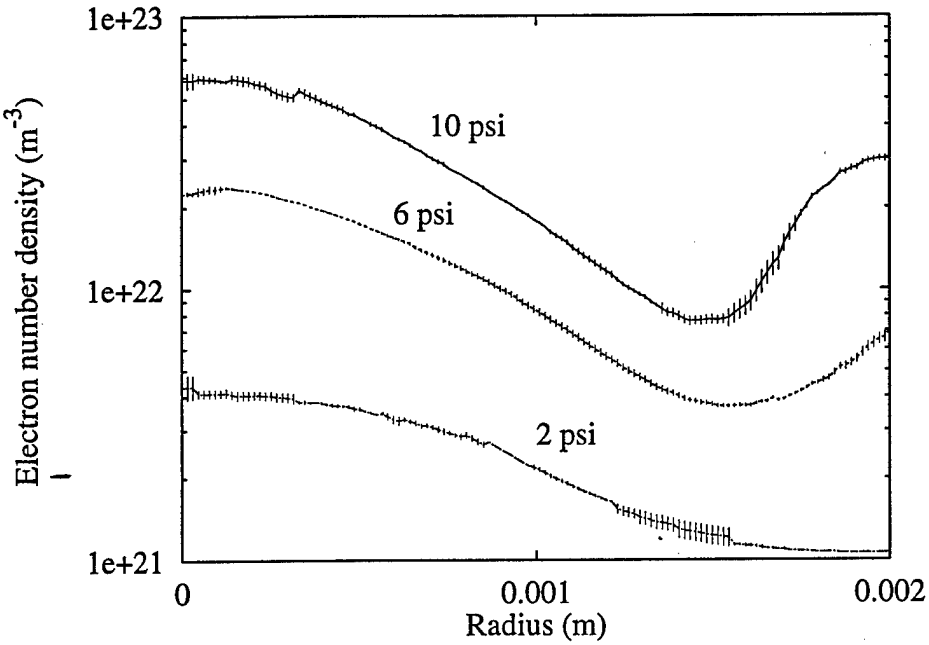


Figure 13. Radial Distributions of Electron Number Densities for Simulated Ammonia ($NH_3$) at 2.0 psi, 6.0 psi, and 10.0 psi.

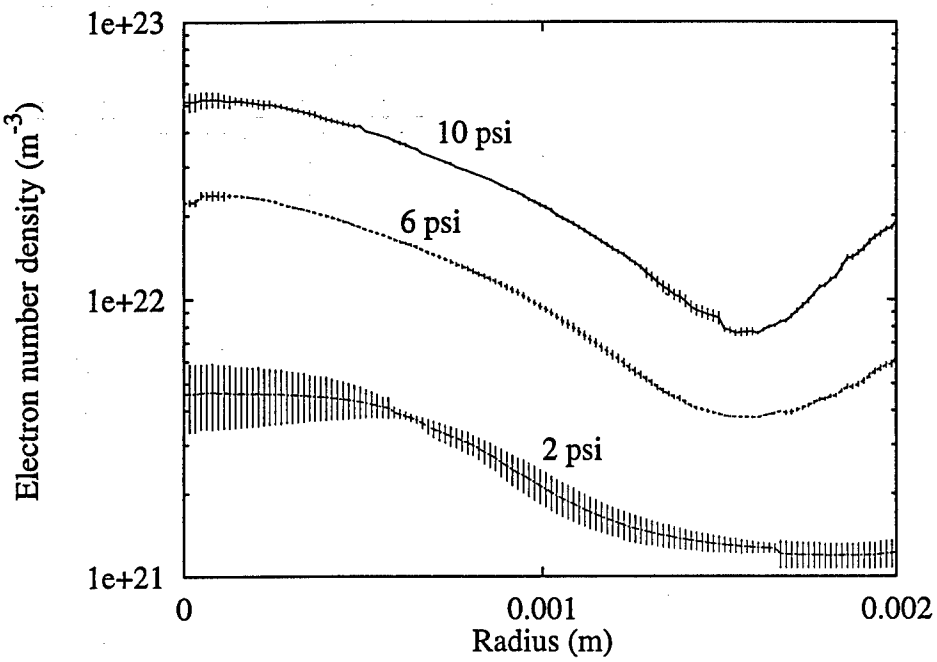


Figure 14. Radial Distributions of Electron Number Densities for Simulated Hydrazine ($N_2H_4$) at 2.0 psi, 6.0 psi, and 10.0 psi.

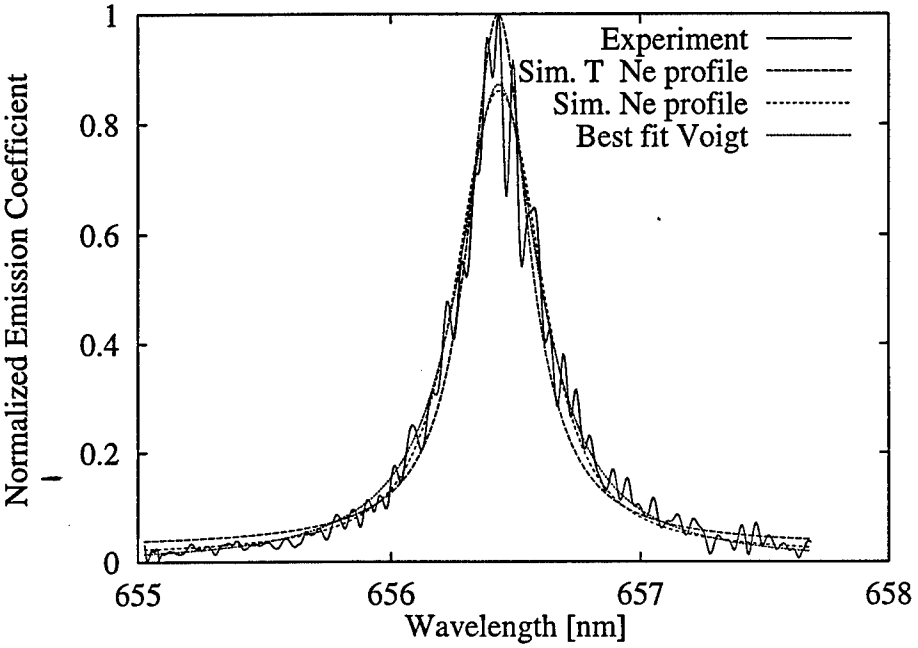


Figure 15 Comparison of "Best fit Voigt" profile and simulated Voigt profiles calculated from the "U of I" simulation results for a 50 Amp hydrogen arc at 6.0 psi at a radius of 0.03 mm.

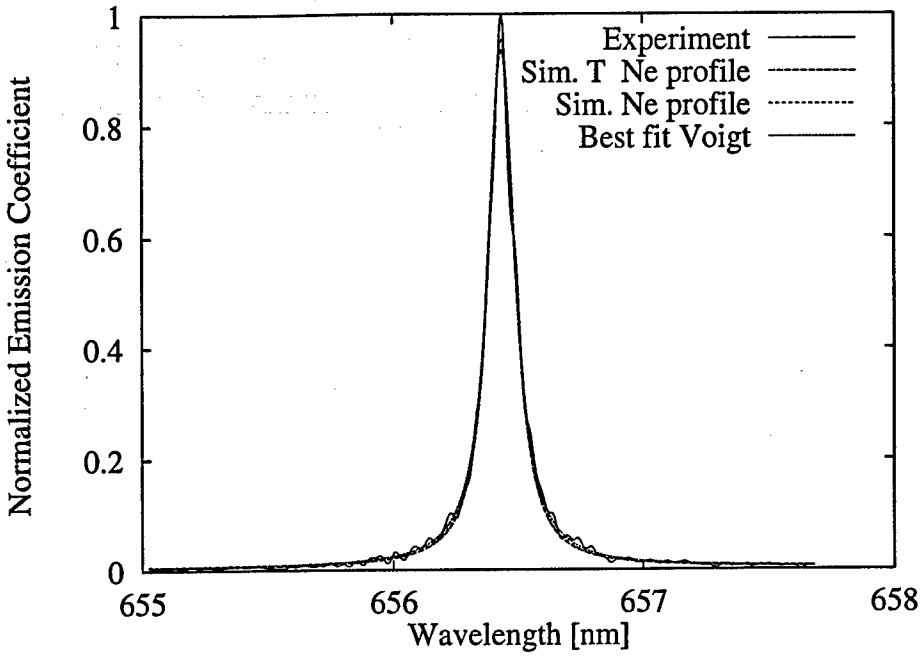


Figure 16 Comparison of "Best fit Voigt" profile and simulated Voigt profiles calculated from the "U of I" simulation results for a 50 Amp hydrogen arc at 6.0 psi at a radius of 1.5 mm.

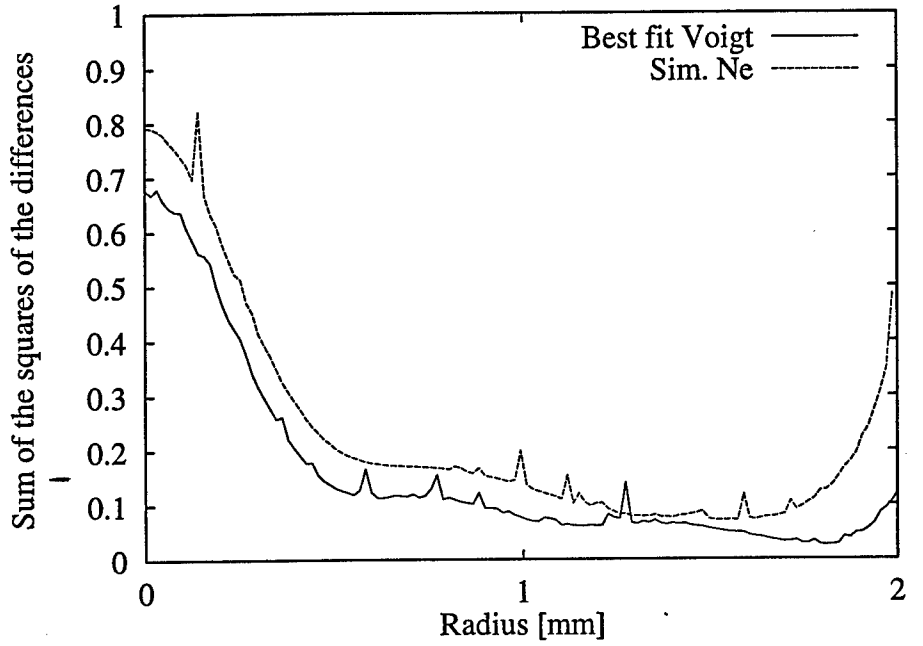


Figure 17 Radial distribution of error associated with the "Best fit Voigt" profile and simulated Voigt profiles calculated from the "U of I" simulation results at 6.0 psi.

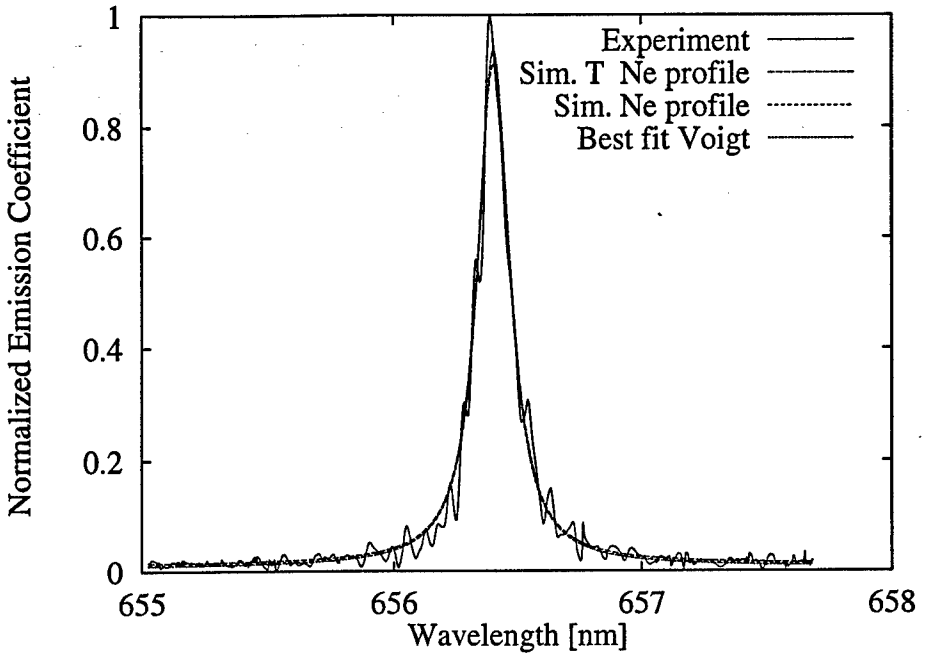


Figure 18 Comparison of "Best fit Voigt" profile and simulated Voigt profiles calculated from the "U of I" simulation results for a 50 Amp hydrogen arc at 2.0 psi at a radius of 0.03 mm.

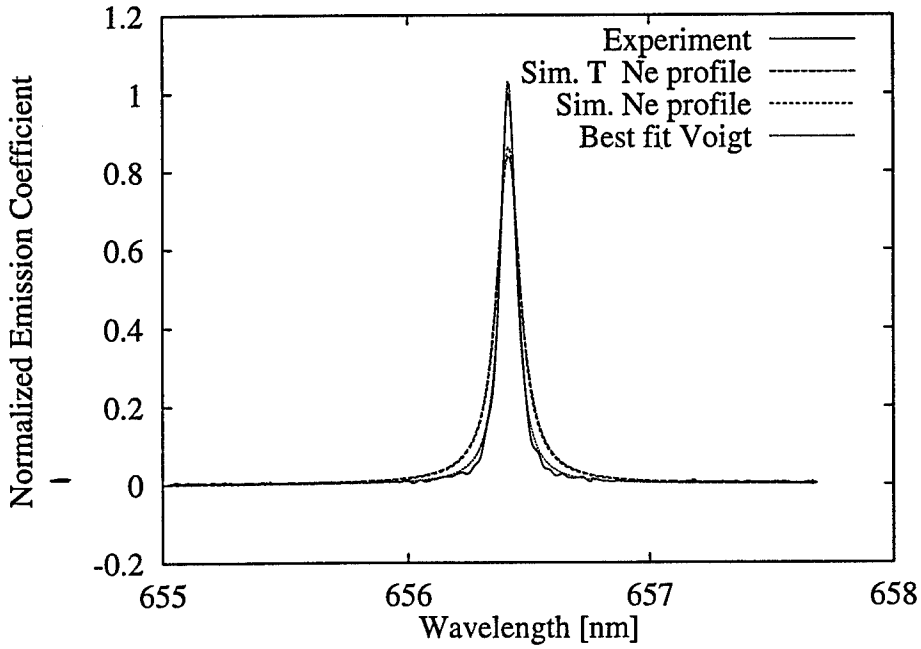


Figure 19 Comparison of "Best fit Voigt" profile and simulated Voigt profiles calculated from the "U of I" simulation results for a 50 Amp hydrogen arc at 2.0 psi at a radius of 1.5 mm.

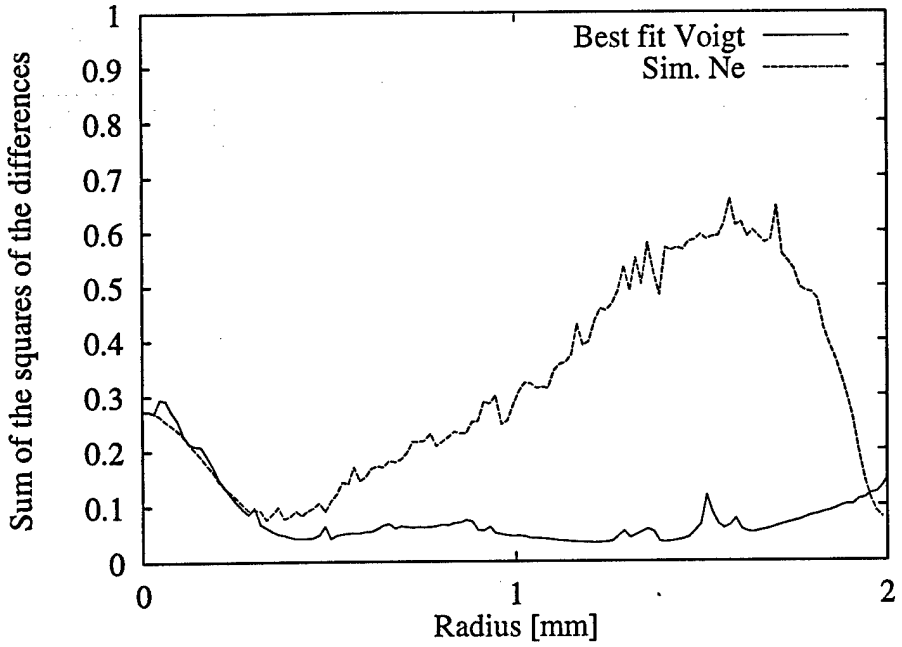


Figure 20 Radial distribution of error associated with the "Best fit Voigt" profile and simulated Voigt profiles calculated from the "U of I" simulation results at 2.0 psi.

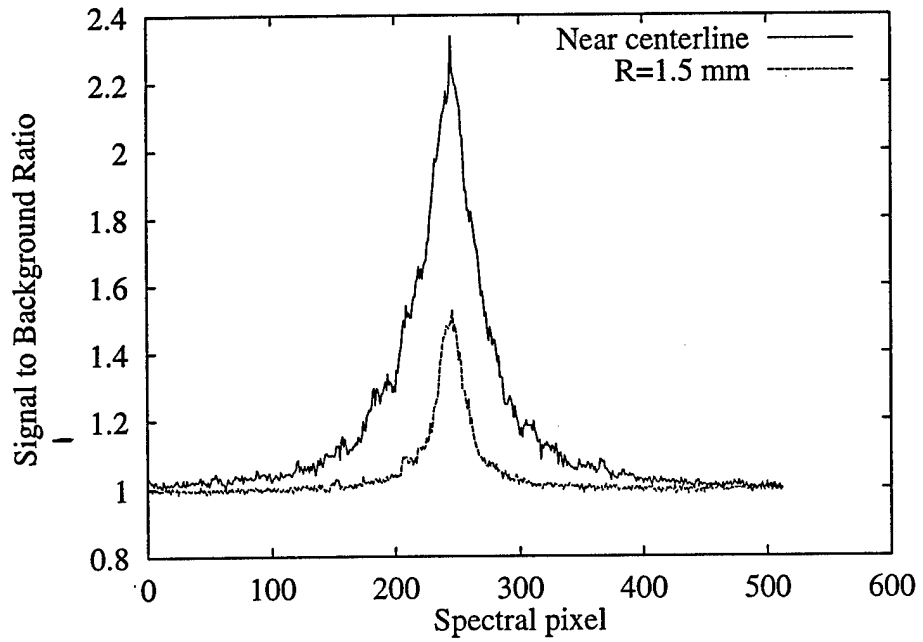


Figure 21 Spectrally resolved signal to background noise ratios of the $H_\alpha$ line intensities near centerline and at a radius of 1.5 mm for a 50 Amp hydrogen arc at 6.0 psi.

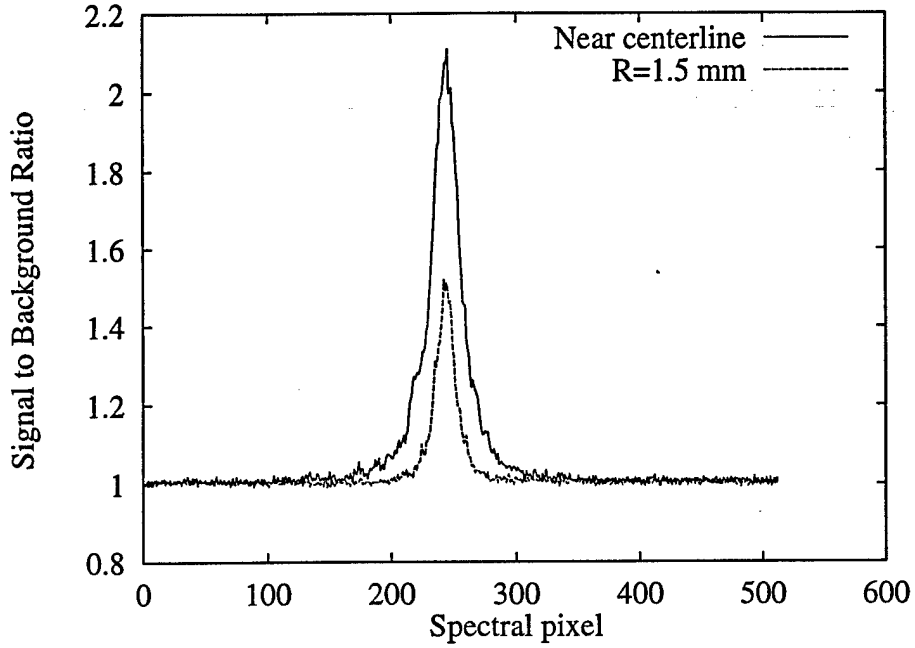


Figure 22 Spectrally resolved signal to background noise ratios of the $H_\alpha$ line intensities near centerline and at a radius of 1.5 mm for a 50 Amp hydrogen arc at 2.0 psi.

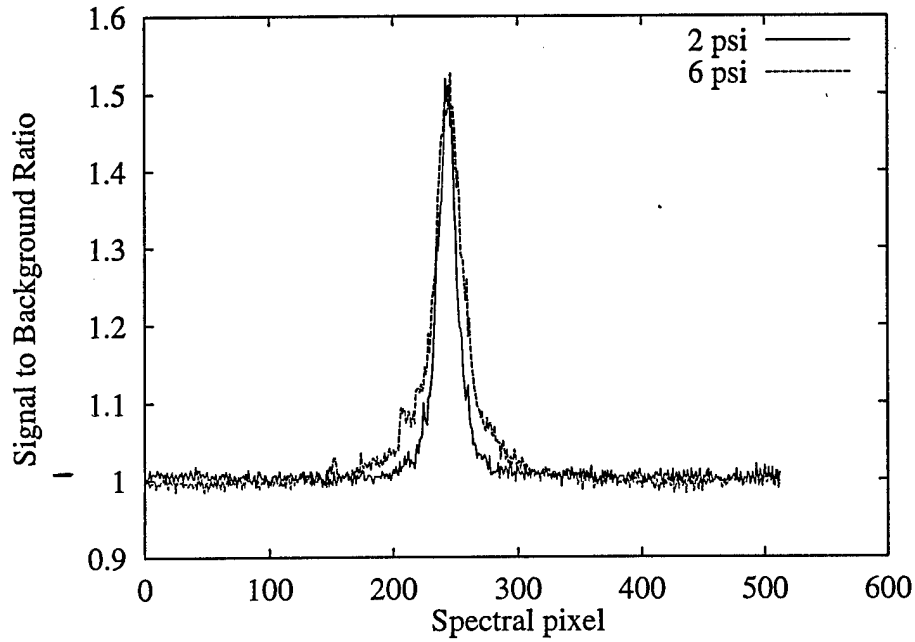


Figure 23 Signal to noise background noise ratio of the spectral $H_\alpha$ line intensity profiles for the 2.0 psi and 6.0 psi hydrogen arcs at a radius of 1.5 mm.